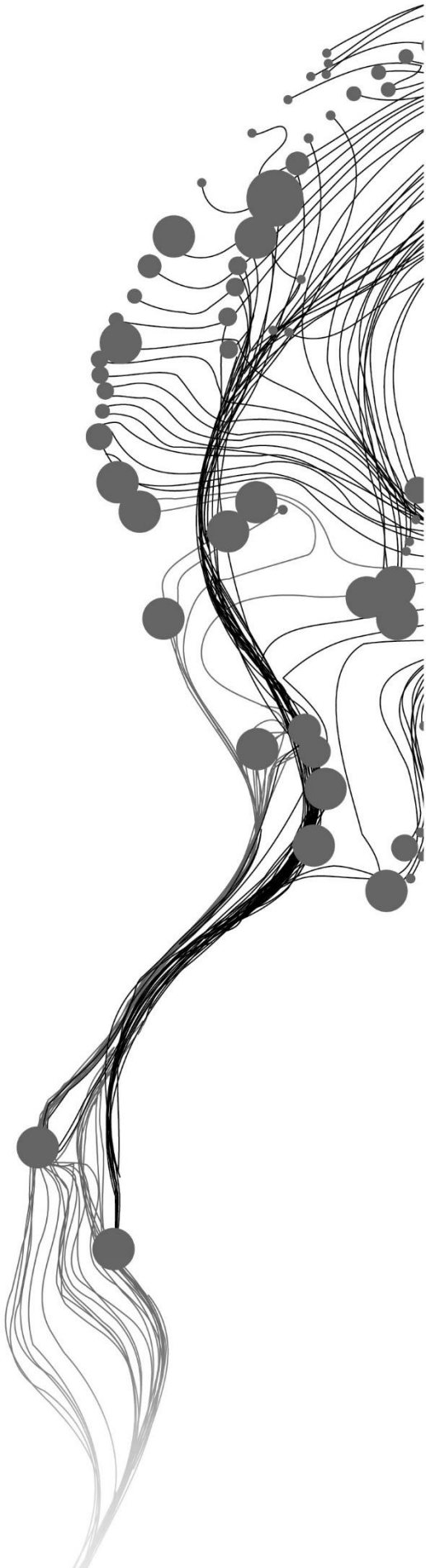# THE MINERALOGICAL AND SPECTRAL CHARACTERISCTICS OF A LITHIUM-BEARING PEGMATITE STSYEM

OKEKE IFEANYI JOHNBOSCO
JULY 2024

SUPERVISORS:
Dr. A.H Dijkstra
Dr. F.J.A Ruitenbeek

THE MINERALOGICAL AND SPECTRAL CHARACTERISTICS OF A LITHIUM-BEARING PEGMATITE SYSTEM

OKEKE IFEANYI JOHNBOSCO
Enschede, The Netherlands, JULY 2024

Thesis submitted to the Faculty of Geo-Information Science and Earth Observation of the University of Twente in partial fulfilment of the requirements for the degree of Master of Science in Geo-information Science and Earth Observation.
Specialization: Applied Remote Sensing for Earth Observations

SUPERVISORS:
Dr. A.H Dijkstra
Dr. F.J.A Ruitenbeek

THESIS ASSESSMENT BOARD:
Dr. J.C Afonso (Chair)
Dr. Rob Hewson (External Examiner, Royal Melbourne Institute of Technology University)]

ABSTRACT

Lithium-bearing pegmatite systems are significant sources of lithium, a critical element in modern energy storage technologies, particularly in the production of lithium-ion batteries. Despite their importance, these types of mineral deposits have been subjected to numerous studies over the years, using a variety of approaches. The analysis of the spectral characteristics can be used to identify the mineralogy with different alteration events associated with granitic intrusions hosting the deposit of lithium-bearing minerals. The occurrence of mineral commodities is usually attributed to geological events, which is why a mineral exploration strategy needs to be developed to identify and describe lithium-bearing pegmatite systems, especially in areas with little or no pegmatite exposure linked to early lithium exploration. Alterations such as metamorphism events can be observed in the visible-near infrared (VNIR) and short-wave infrared (SWIR) spectrum.

This research combines laboratory measurements and airborne geophysical datasets to identify and describe a known lithium-bearing pegmatite system in Southwestern England. It aims to analyze the spectral characteristics and mineralogy using an integrated approach of SWIR imaging spectroscopy, VNIR-SWIR spectroscopy, portable X-ray Fluorescence (XRF), X-ray Diffraction (XRD), and magnetic susceptibility with airborne radiometric and magnetic datasets. The laboratory data has proven useful for identifying small features such as aluminous micas, tourmaline, biotite, and topaz in the granite and pegmatite samples while the airborne radiometric and magnetic data improve the identification and characterization of larger features such as granitic plutons.

The wavelength maps in the SWIR range were used to identify and map the aluminous micas; muscovite, and illite using the shift in the Al-OH absorption characteristics to determine the spectral mineralogy which includes muscovite, illite, topaz, tourmaline, and biotite. VNIR-SWIR spectroscopy provided useful information, especially in the VNIR region of the spectrum, which allowed lithium-bearing micas like zinnwaldite and lepidolite to be identified. In this study, the stacked spectra of the samples obtained from each component, based on the type level, provided information about the trend in the fractionation process that led to the deposit of minerals.

XRD analysis provided insight into the identification of minerals like quartz and feldspars and was compared with the results of the spectral analysis. The radiometric and magnetic signatures provided useful information for improving the characterization of the larger features in the lithium-bearing pegmatite system. The results from the spectral mineralogy and chemical variations showed the progressive fractionation and evolution of batholith granites, topaz granites, and aplite pegmatite from the parent magma.

This study demonstrates that by integrating these diverse analytical methods a more robust identification and characterization can be achieved by addressing the limitations of individual methods.

ACKNOWLEDGEMENTS

I wish to say thank you to the staff of the Faculty of Geo-Information Science and Earth Observation (ITC) at the University of Twente. Your expertise, dedication, and willingness to assist have been invaluable. The high-quality education and resources provided have significantly contributed to my academic growth.

I would also like to extend my heartfelt thanks to the Netherlands University Foundation for International Cooperation (NUFFIC) for providing the financial support necessary for my studies. This opportunity has been life-changing, and it would not have been possible without your generosity.

I am grateful to my supervisors, Dr. Arjan Dijkstra and Dr. Frank van Ruitenbeek. Your insightful feedback, patience, and encouragement have been crucial to shaping this thesis. Your commitment to my academic and professional development has been truly inspiring.

A special thanks to the ITC geoscience laboratory staff Camilla Marcatelli and Kathrin Zweers-Peter for their continuous support and assistance during laboratory measurements.

To my wife Helen and kids Michael, and Stephanie, and friends I met in the Netherlands and back in Nigeria, your unwavering support and encouragement have been my bedrock. Thank you for your understanding, patience, and belief in me, especially during the most challenging times. Your love and support have been my driving force.

Lastly, I want to thank my fellow students and classmates for the camaraderie, knowledge exchange, and memorable experiences we have shared. Your friendship and support have made this journey enjoyable and enriching.

Thank you all for your contributions and support. This achievement would not have been possible without you.

TABLE OF CONTENTS

LIST OF FIGURES

LIST OF TABLES

1. INTRODUCTION

1.1. Background and Justification

The demand for Lithium (Li), one of the critical elements in rechargeable battery production, has witnessed rapid growth because of the tremendous surge in electric vehicles and renewable energy technologies (World Bank, 2020). To address this demand, there is a need to identify and evaluate new European Li deposits that have emerged as significant lithium sources, attracting considerable attention from the energy and transportation industries (Gourcerol et al., 2019; European Union, 2020).

Pegmatites are intrusive igneous rocks that form from highly fractionated, water-enriched magmas. They are renowned for their exceptional mineral diversity and often host economically valuable lithium-rich minerals. These lithium-bearing pegmatite systems typically occur in association with granitic intrusions and their unique mineralogy and geological settings make them prime targets for lithium exploration (Zimanovskaya et al., 2022).

Understanding the unique composition and mineralogy of granitic intrusions associated with known lithium-bearing pegmatite systems can help locate other geological settings/systems where the pegmatite itself is not exposed or only a little of the components are exposed. In this proposed study, a known geological setting with lithium-bearing pegmatite will be used as a field laboratory to study the composition and mineralogy of the pegmatite and the associated granitic intrusive rocks that will provide valuable information in early-stage lithium exploration.

The mineralogical composition of rocks and minerals can be studied using their electromagnetic spectrum characteristics, particularly in the visible-near-infrared (VNIR), shortwave infrared (SWIR), and longwave infrared (LWIR) by providing the background for the interpretation of the spectroscopic data (Rajesh, 2004). Hence, by analyzing the spectral signatures of lithological units and mineral assemblages within the lithium pegmatite system, it is possible to identify and map the distribution of different minerals within the lithium pegmatite system (Cardoso-Fernandes et al., 2021). This spectral information can be used to identify similar geological systems in large-scale exploration programs that use remote sensing methods. It enables cost-effective exploration and identification of regions that might have lithium deposits in economic quantity (Chen et al., 2023).

Several authors have studied the detection of lithium-bearing pegmatites using different methods. Muller et al. (2023) highlighted some of the tools and techniques useful for identifying pegmatite ore bodies formed as the advancement of an integrated toolset from the GREENPEG project, which is aimed at enhancing

the identification of buried European pegmatite ore bodies. However, these methods have been successful in identifying pegmatite ore bodies in areas where there is sufficient exposure to pegmatite. Keyser et al. (2023) recently analyzed the trace element concentrations of quartz from LCT (Li Cs Ta) pegmatites in Austria and Ireland. This research provided useful information for Li-mineralization and access to the pegmatite chemical signatures. However, the study was carried out where there was sufficient pegmatite exposure. Aside from the geochemical techniques, other methods have been evaluated. Another important approach is the hyperspectral remote sensing technique of imaging spectroscopy, Rajesh (2004) provides the importance of using reflectance spectroscopy to delineate minerals of interest. Cardoso-Fernandes et al. (2021) employed reflectance spectroscopy to identify the different lithological units of pegmatite in the Fregeneda–Almendra, this method successfully used the distinct absorption features to provide useful information on the spectral behaviours of the Li mineralization of the pegmatite. This study, however, is useful in areas with pegmatite exposure.

Cardoso-Fernandes et al. (2023) as part of an effort by the European Commission towards identifying the European pegmatite ore deposits added new properties of pegmatite using reflectance spectroscopy studies to create a database for pegmatite samples from Austria, Norway, Ireland, Portugal, and Spain. However, this is useful for exploration in areas where the pegmatites are sufficiently exposed. Cardoso-Fernandes et al. (2023) recently focused on the evaluation of spectral signatures of targets from the pegmatite dykes located in the Barroso–Alvão pegmatite field using an integrated remote sensing approach with a geophysical survey (gamma-ray spectrometry) and spectral data of rock samples from the field. This method, despite the limitation in the spatial resolution of the data, was successful in identifying the pegmatites but only useful in areas where there is sufficient pegmatite exposure.

Due to the limited successes of the studies discussed above, a new approach is needed because the previous studies are focused on areas with sufficient pegmatite exposure. The research gap is the challenge of detecting Li-bearing pegmatites in areas with little or no pegmatite exposure, this study will provide useful information for early exploration by considering the entire Li pegmatite system, unlike the previous studies. Hence, with the increasing development of exploration technologies for the discovery of lithium deposits, there is a need to develop a conceptual model for identifying lithium pegmatite systems. A mineral system analysis approach provides this conceptual framework for understanding geological evolution leading to diverse mineral deposits. This approach differs from other approaches because it focuses on the entire geological processes at the source of the deposit of the minerals rather than individual deposits (Sweetapple, 2017). This methodology relies more on its application using spectral datasets to detect the smaller features of the granites and pegmatites, with the integration of geophysical datasets for detecting the larger reservoirs from which the pegmatite fluid is formed by fractionation processes. These larger features have a bigger chance of being detectable by spectral and geophysical methods.

Therefore, given the importance of lithium-bearing pegmatite systems as sources of lithium, there is a critical need to develop a multi-observable model for identifying and describing minerals in a Li pegmatite system. This research can address this need by integrating spectral data with geophysical datasets (radiometric and magnetic) from Southwestern England.

The rocks of southwestern England are considered for this research because of their geological settings which are known to be associated with granitic intrusions with a long history of magmatic and hydrothermal activities conducive to the formation of pegmatites and associated mineralogy, which allows a mineral system approach to provide an understanding of the relationship between Li-bearing pegmatites and the large fractionating magma reservoir, focusing on its mineralogy and spectral properties. Thereby establishing a strong genetic linkage between the rocks in southwestern England that comprise the large batholith that fractionates into a larger magma reservoir from which other components; topaz granite, leucogranite, and pegmatites are formed, providing an understanding of the magmatic evolution of the different rock types (Breiter et al., 2016; Simon et al., 2016). Also, with a rich history of mining activities as well as the discovery in 2018 of a significant lithium deposit by British Lithium, the first company to drill for lithium in the UK, and the potential for future use of renewable energy sources for metal extraction processes in Cornwell by Cornish Lithium, the rocks in southwestern England make an excellent study area for further research into early lithium exploration (British lithium, n.d.; Cornish lithium, n.d.).

This is a complete Li pegmatite system (Fig.1.1) in southwestern England that shows all the different components (batholith, topaz granite, leucogranite, and pegmatite) that can provide useful information even in areas without pegmatite exposure. Hence, to improve the unique characterization of laboratory measurements on collected samples, fully processed airborne magnetic and radiometric data will be integrated.

Therefore, this research aims to use spectral characteristics based on the absorption features from the spectral signatures and geophysical datasets to classify the lithium-bearing pegmatite system. The results of this research will be used to identify other Li pegmatite systems based on their spectral characteristics and mineral composition. For the mining industry, these will provide transferrable information useful for identifying and assessing potential Li pegmatite systems, especially in areas with little or no pegmatite exposure.
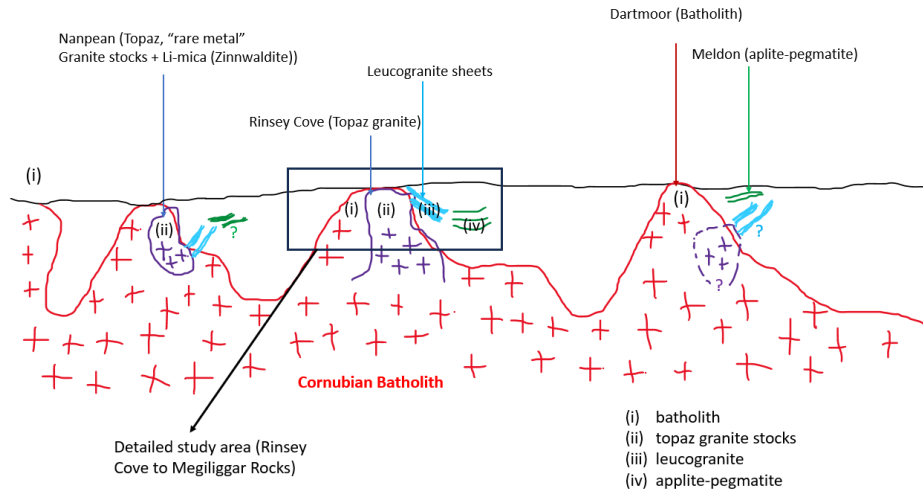
Figure 1.1: Schematic cross-section through the SW of England showing the Cornubian batholith, leucogranite, topaz granite, and pegmatite components of the system (A. Dijkstra, personal communication)

1.2. Research Objectives

1.2.1. Main Objectives

The main objective is to develop a descriptive, multi-observable model using spectral, radiometric, and magnetic airborne geophysical data to identify several parts of a lithium-bearing pegmatite system based on the granitic and pegmatitic rocks from Southwestern England.

1.2.2. Specific Objectives

1. To determine the spectral characteristics and typical mineralogy in the system from the rock samples available in the laboratory using X-ray diffraction (XRD), X-ray Fluorescence (XRF), magnetic susceptibility, VNIR–SWIR spectroscopy, and SWIR imaging spectroscopy.
2. To analyze the airborne radiometric and magnetic datasets and interpret radioelement variation and magnetic relief in the various parts of the system.
3. To integrate all the results from the laboratory measurements, airborne radiometric, and magnetic datasets and develop a model for recognizing each of the components based on the multi-observables/signatures.

1.2.3.   Research Questions

1. How does the mineralogy of the rock samples vary with different rock types in the system?

2. What is the spectral mineralogy of each rock type in the SWIR imaging spectroscopy?

3. How does the radiometric and magnetic susceptibility vary with different rock types in the system?

4. How can a descriptive, multi-observable framework be structured to represent the relationships between the different components based on their radiometric, magnetic, and spectral signatures?

5. How to effectively integrate spectral, radiometric, and magnetic sets of signatures/observables to create a model for recognizing each component of the system?

1.3. Geologic setting of Southwestern England

The lithium-bearing pegmatite system rocks located in Southwest England (Fig. 1.2) are characterized by rich mineral resources and have a history of mining activities for deposits such as tin, copper, kaolinite, and arsenic production (Price et al., 2005). It is composed of rocks of peraluminous granites that intruded at the end of the Variscan convergence that occurred in SW England during the late Paleozoic era (Carboniferous to early Permian period). This orogeny resulted from the collision between North America and part of Europe with the Gondwana creating thrusting, faulting, and folding which resulted in the development of the Cornubian batholith granite intruding into the sedimentary rocks, extending from Dartmoor to Isles of Scilly with associated mineralization in Cu, Sn and the extraction of other metals like Fe, U, Pb and As (Simons et al., 2016; Dijkstra and Hatch, 2018; Smith et al., 2019; Searle et al., 2024). The residual melts of this granitic intrusion form into the pegmatites which hosts lithium and various rare earth metals such as Ta and Nb. The region also comprises rocks of Carboniferous and Devonian age which are of sedimentary origin with intense metamorphism and abundant in sandstones, slates, and limestones deposited in the marine environment during and after the Variscan orogeny (Searle et al., 2024). The post-orogenic erosion during the tertiary and quaternary resulted in the emplacement of the Cornubian batholith granites and deposits of alluvial and fluvial sediments covering the old geology bedrock. The intrusion of the Cornubian batholith generated metamorphic aureoles due to contact metamorphism (Shail et al., 2003). According to Jacob et al., (2021), a similar type of granite and mineralization exists in parts of Europe like Portugal, Spain, France, the Czech Republic, and Canada.
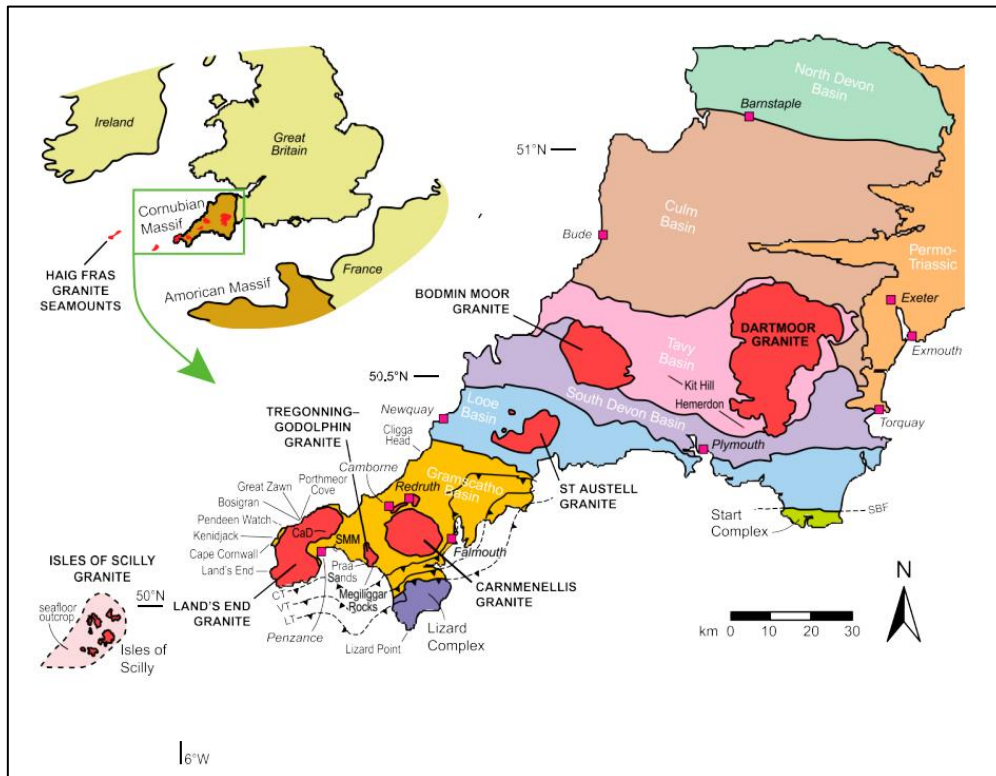
Figure 1.2: Geological map of SW England showing the granite plutons (Searle et al., 2024)

The Variscan post-collision peraluminous granite in the region according to Simons et al. (2016, 2017) can be divided into five major types; two mica (G1), muscovite granite (G2), biotite granite (G3), tourmaline (G4) and (G5) topaz granite (Fig. 1.3). The two mica granites are formed by muscovite with little biotite due to the dehydration of the melting of a greywacke source. Muscovite granite is peraluminous granite formed by fractionation hosting Tn and W mineralization with enrichment in rare earth elements (REEs). An increased tourmaline due to the dehydration melting of biotite formed by the biotite granites at slightly higher temperatures with lower pressure (Müller et al., 2006). The tourmaline granites are derived by fractionation of the biotite granites and are enriched in tourmaline schorl and lithium-bearing micas (Williamson et al., 2000). Fig. 1. 4 illustrates that the topaz granite (G5a) associated with aplite pegmatite (G5b) are enriched in tourmaline, lithium-bearing micas (zinnwaldite, lepidolite) and are related to the other granites (G2, G3) by fractional crystallization (Simons et al., 2016; Breiter et al., 2018). As observed in Fig. 1.4, a good fractionation trend exists from the batholith granites (G2, G3), and topaz granite (G5b) to the pegmatites (G5b).
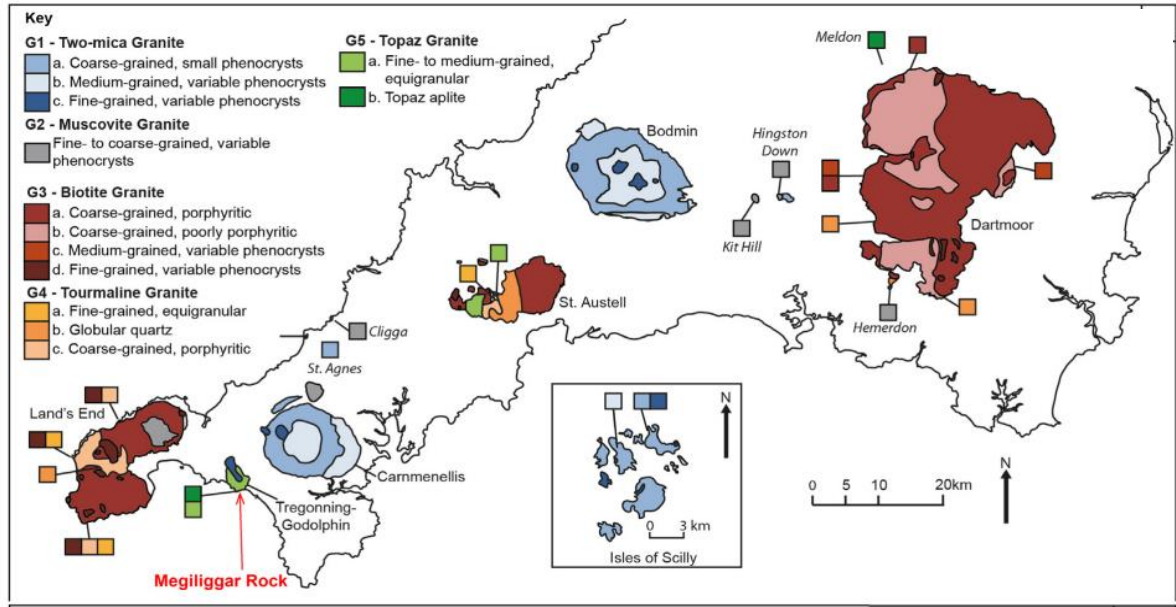
Figure 1.3: Geological sketch map of the granite plutons showing the different granite types (Simons et al., 2016)
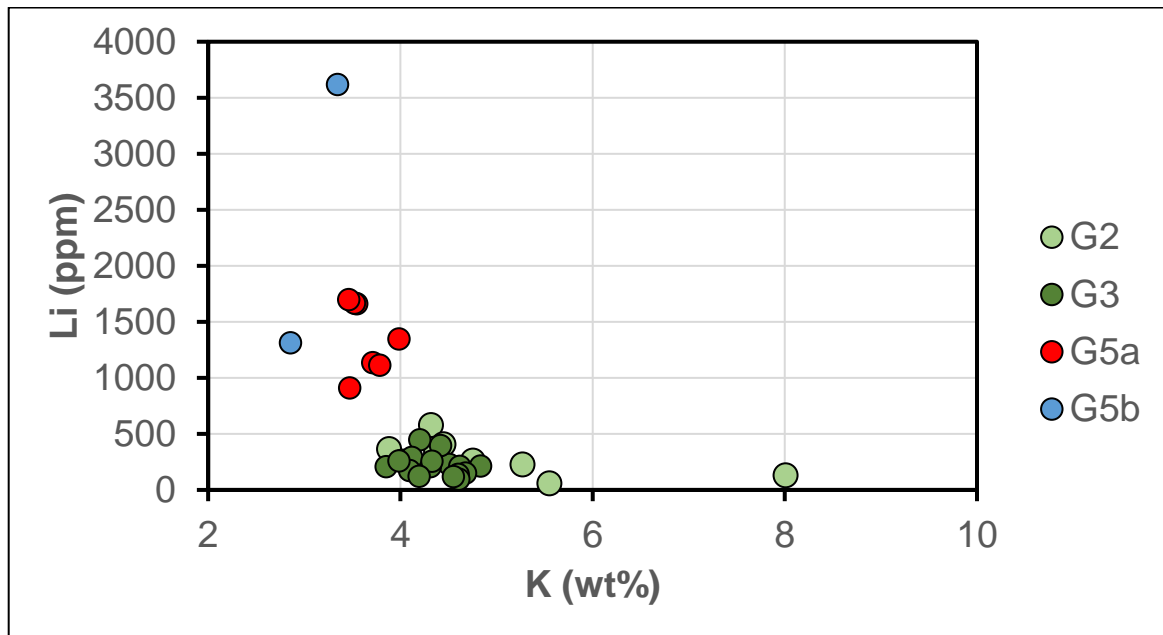
Figure 1.4: Lithium against potassium concentrations. Circles represent data from Simons et al. (2016, 2017) G2 and G3 granites are batholith granites; G5a are topaz granites; G5b are aplite-pegmatites.

1.4. Structure of the thesis

This thesis is made up of seven (7) chapters and is briefly described below:

Chapter One is an introduction and describes the research background and justification, objectives, research questions, and the geologic setting of SW England. Chapter Two provides datasets and methods. It also describes the research methodology required to achieve the research objectives and provide answers to the research questions. Chapter Three presents the results of imaging and reflectance spectroscopy. Chapter Four presents the results of XRD, XRF, and magnetic susceptibility. Chapter Five presents the results of airborne geophysical data. Chapter Six presents the integration of results from the laboratory and airborne geophysical datasets and a description of the multi-observable model. Chapter Seven is the discussion, conclusion, and recommendations.

2. DATASETS AND METHODS

The main datasets used in this study are granite and pegmatite rock samples. This section describes the different datasets, methods of sample preparation, analytical methods, and already processed airborne geophysical data required to achieve the research objectives and provide the needed answers to the research questions (Fig. 2.1).
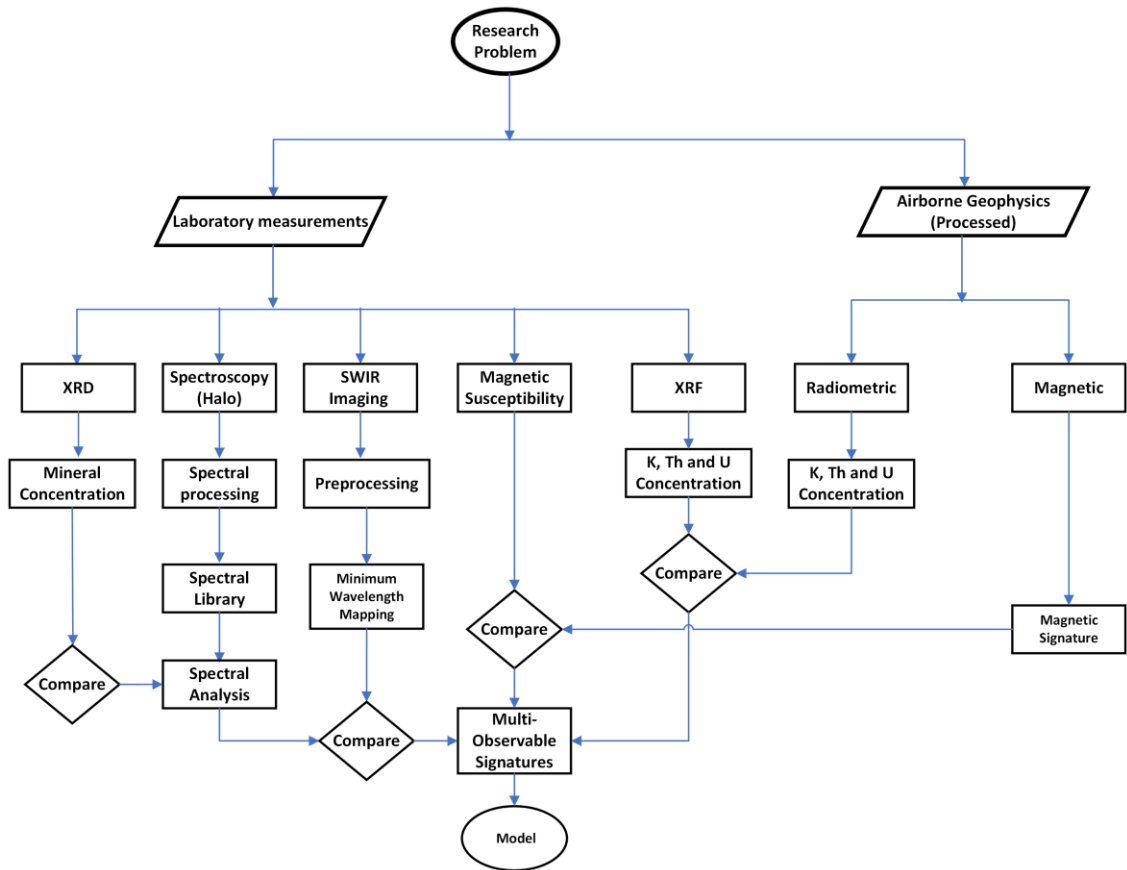
Figure 2.1: Research methodological flowchart

2.1. Datasets

This study was based on the analysis of SPECIM SWIR imaging spectroscopy, VNIR-SWIR reflectance spectroscopy, and XRD, with the combination of XRF, magnetic susceptibility, airborne magnetic and radiometric processed datasets for comparison.

2.1.1. Rock samples

A total of sixteen (16) rock samples were used for this study, including twelve (12) granite samples and four (4) pegmatite samples. In this study, five (5) granite samples were selected from batholith granite, seven (7) granite samples from topaz granite, and four (4) pegmatite samples from aplite pegmatite components. These rock samples were collected by Arjan Dykstra during research visits to various locations in Southwestern England. Their locations and images can be found in Appendix I and II. All rock samples were prepared and milled for XRD analysis.

2.1.1.1. Sample preparations for XRD analysis

The granite rock samples from the batholiths were initially sawed using the sawing-machine and dried for 24 hours in the oven before milling. Other rock samples (topaz granite and pegmatite) were hammered, and all samples were milled using a planetary ball milling machine. Each sample weighed around 8 grams in the grinding jar to ensure balance in the planetary ball milling machine (Fig. 2.2a and b). The milling time was 10 minutes with a maximum speed of 350 and 400 rpm for topaz granite and pegmatite/batholith granite respectively to avoid destroying the crystals and the grain size is 10-100 μm.
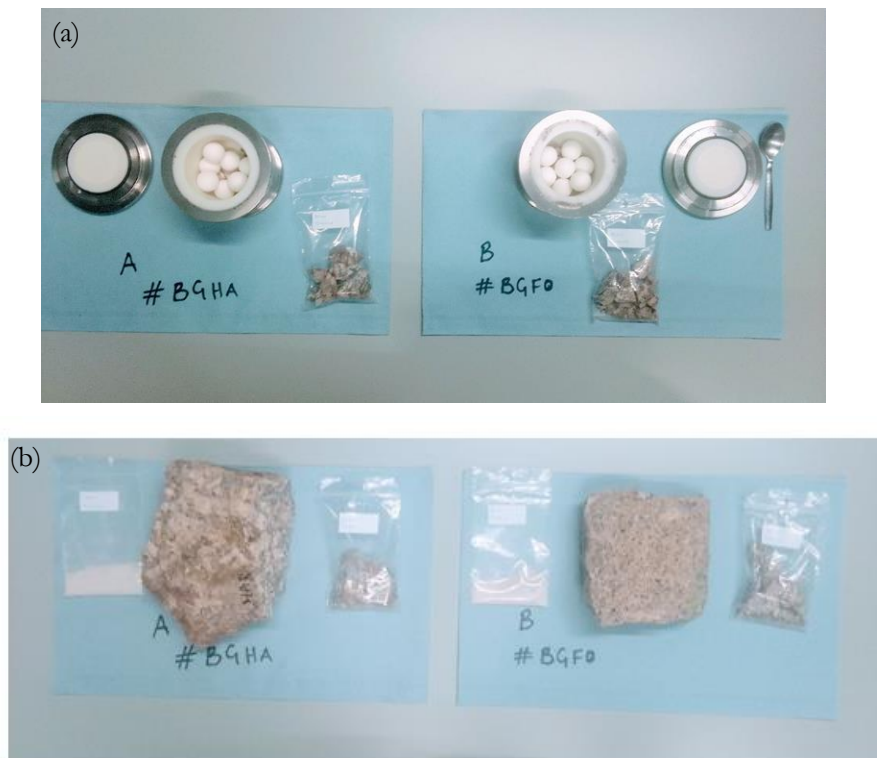
Figure 2.2: Shows sample preparation for the XRD analysis. Sample in the grinding jar (a) and sample after milling (b)

2.1.2. Airborne geophysical data

According to Beamish et al. (2014), the fully processed Tellus SW airborne geophysical datasets (magnetic and radiometric) were acquired over the counties of Cornwall and parts of Devon and Somerset between 1 August 2013 and 02 January 2014. The data acquisition was undertaken by CGG Airborne Survey (Pty) Ltd (formerly Fugro Airborne Surveys) on behalf of the British Geological Survey. This survey comprises a high-resolution magnetic gradient with a 256 radiometric multichannel, a line spacing of 200m (about 656.17 ft), a tie-line spacing of 2000m (about 1.24 mi), and a line orientation of 0 degrees.

2.1.2.1. Airborne magnetic data

The airborne magnetic data was used in already processed form (GeoTIFFs). The raw data had previously been de-spiked and then decimated to 20 Hz. To remove the system parallax and heading a time offset was applied to the Scintrex CS-3 magnetometer that records the magnetic intensity, magnetic gradient, and other altitude instruments at various locations recording away from the aircraft position. These will restore the data to the current time and location. The magnetic data was gridded into a 40m grid cell size using a bi-cubic spline (Beamish et al., 2014).

2.1.2.2. Airborne radiometric data

Similarly, the airborne radiometric data was used in already processed form (GeoTIFFs). The values of potassium, thorium, uranium, and total count of the raw data were filtered using a Gaussian low pass filter to remove cosmic and aircraft background. Energy calibration, dead time correction, and selection of regions of interest were performed in the field. Other processing performed includes radon background removal, calculation of effective height, spectral stripping, height correction, conversion to concentrations, leveling, and noise-adjusted singular value decomposition (NASVD) for enhancing the low signal-to-noise regions of interest (Beamish et al., 2014). More information about the airborne geophysical survey report with details of the data processing can be found at www.tellusgb.ac.uk.

2.2. Analytical methods

To analyze the spectral characteristics and elemental concentrations of the rock samples, various analytical methods were carried out. These methods include VNIR–SWIR reflectance spectroscopy, SWIR imaging spectroscopy, X-ray diffraction (XRD), X-ray fluorescence (XRF), and magnetic susceptibility. These methods are described in the following sections.

2.2.1. Spectroscopy

To identify the surface mineralogy and determine the spatial distribution of the occurrence of tourmaline, biotite, topaz, muscovite, and illite associations in the lithium-bearing pegmatite system, the first step of processing the spectral data was mapping the wavelength position and depth of absorption features at a wavelength range between 2100-2400 nm (van Ruitenbeek et al., 2014) using a Wavelength Mapper (HypPy) developed by the Faculty of ITC, University of Twente, Enschede, the Netherlands.

To improve the level of detail on the overview of the mineral association and show the differences between the mineralogy present, an additional wavelength map ranging between 2180-2225 nm was created (described in more detail in the following section). To show the difference between muscovite and illite, a muscovite-illite crystallinity image was created using the +/- 1900 nm water feature and the +/- 2200 nm of the Al-OH feature (Hecker et al. 2019c). To identify and compare minerals such as lepidolite, zinnwaldite, and muscovite with absorption features in the VNIR-SWIR range (400-2500 nm), a broad spectral range was collected to provide differences for minerals such as muscovite and lepidolite which have similar absorption features in the SWIR range. This step presents an overview of the types of minerals expected in the lithium-bearing pegmatite system (Fig. 2.3).
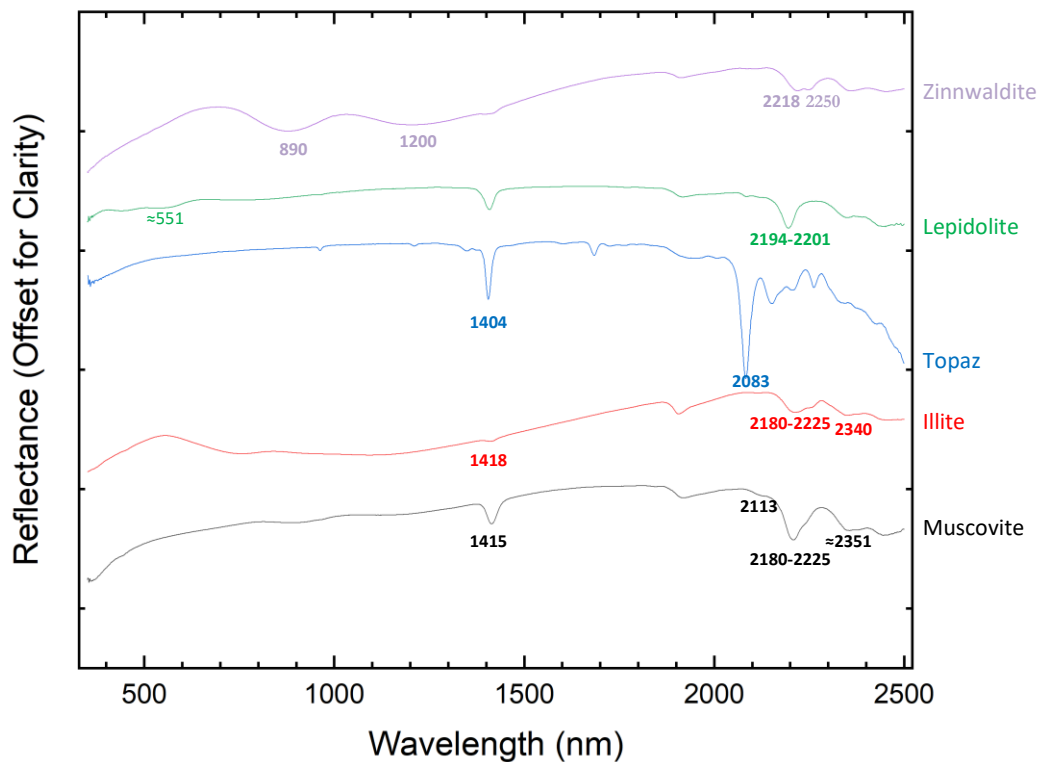
Figure 2.3: Spectral profile of the expected minerals that are active in the 2100-2400 nm wavelength range from the USGS spectral library (Kokaly et al., 2017; Clark et al., 2007; Mekonnen, 2023)

As observed in Fig. 2.3, each spectral shows different diagnostic absorption features useful for identifying the several types of minerals expected in the lithium-bearing pegmatite system.

2.2.1.1. SWIR Imaging Spectroscopy

SWIR imaging spectroscopy was carried out to determine its application in identifying minerals and mapping the mineral composition using the variation in the spectra obtained from each rock sample. The SWIR SPECIM hyperspectral camera with an OLES30 lens in the ITC geoscience laboratory was used to acquire images of twelve (12) granite and three (3) pegmatite rock samples. The SWIR image acquisition involved scanning all the rock samples within the SWIR (1000 – 2500 nm) wavelength range with a spectral resolution of 12 nm, and 256 µm pixel size.

After image acquisition, to remove noisy backgrounds the image was spectrally subset by removing the noisy bands (bands 1-16 & 288) at the starting and ending of the wavelength range using ENVI version 5.7 software. To maintain the region of interest, spatial sub-setting was applied to create each sample from the mosaicked image. Next, the minimum wavelength image was created by setting the wavelength range from 2050-2400 nm using the wavelength mapper (step 1) to determine the interpolated wavelength position of the deepest absorption feature and interpolated depth. In the wavelength mapper step 2, a spectral subset and depth stretch were defined to produce wavelength maps to provide an overview of the minerals in each sample. All samples were produced using a spectral subset 2180-2225 nm with automatic depth stretching. To highlight samples with the features of topaz, a wavelength map was created with a spectral subset of 2079-2086 nm, and a depth stretching of 0-50% was applied to increase contrast, show more features with topaz, and reduce background noise from other features (Hecker et al. 2019c). An additional wavelength map was created with a spectral subset of 2250-2260 nm to highlight the features of biotite. Finally, to show the difference between illite and muscovite features, an illite-muscovite image was created using the band math tool in HypPy software. Firstly, a minimum wavelength image of the wavelength range 1850-2000 nm was created. Next, the band math tool was used to ratio the already created minimum wavelength in the initial step with a spectral subset of 2050-2400 nm with the 1850-2000 nm created minimum wavelength image. The product of this is the illite-muscovite crystallinity image. Lastly, in hyperspectral images a vertical band could be observed running through the center of the image, this is a result of the artifacts due to the cooling of the camera.

2.2.1.2. VNIR – SWIR Reflectance Spectroscopy

The VNIR – SWIR spectral characteristics of the sixteen (16) rock samples were acquired using the ASD TerraSpec HALO spectrometer in the wavelength range of 350–2500 nm with spectral resolutions of 3nm @700 nm, 9.8 nm @ 1400 nm and 8.1 nm @ 2100 nm. The measurements were carried out on rock samples in the ITC geoscience laboratory. The bulk reference spectrum was obtained in the VNIR (400–1300 nm) and SWIR (1300–2500 nm) using an average spectrum from four (4) measurements at the same spot for each rock sample. Before carrying out each measurement, a white reference was used to ensure that the instrument was working optimally.

2.2.2. X-ray Diffraction (XRD)

The XRD measurement was carried out to determine the elemental concentration of the minerals. The measurements were obtained using a Bruker D2 Phaser X-ray diffractometer in the ITC geoscience laboratory. The powdered samples from the rock samples were prepared using an XRD specimen holder. The diffractogram was measured using 6 to 80° 2theta, an increment of 0.012, 0.6 divergence slit, 1mm (about 0.04 in) knife, 8mm (about 0.31 in) detector slit, and an average time per measurement of 656.6 seconds (about 11 minutes) equivalent to 11 scans per sample. After the measurement, the DIFFRAC.EVA software was used to match and determine the minerals associated with each diffractogram from each sample.

2.2.3. X-ray Fluorescence (XRF)

The XRF measurement was carried out to determine the concentration of potassium (K), thorium (Th), and uranium (U) in each of the rock samples. The measurements were obtained using a portable handheld XRF (pXRF) Niton XL3t in the ITC geoscience laboratory. To detect the values of K, Th, and U, the pXRF was set to All Geo mode because of the ability of the mode to detect lighter and heavier elements. The Kaolinite sample was used as a standard to assess the accuracy of the instrument. The potassium concentration of the kaolinite sample is 1.53 wt% and compared with an in-house potassium concentration value of 1.57 wt%. Four (4) measurements were recorded at different spots on each rock sample and an average was determined for each sample. The values obtained will be compared with the radiometric data from the airborne geophysical survey datasets.

2.2.4. Magnetic Susceptibility

The magnetic susceptibility measurement was conducted to determine each rock sample's magnetic susceptibility and measured in 10^{-3} SI units. The measurement was obtained using a handheld KT-10

magnetic susceptibility/conductivity meter from the ITC geoscience laboratory. These measurements were carried out in front of the ITC Faculty building to avoid magnetic interference. The magnetic susceptibility of each rock sample was measured twice (2), and the average was calculated and recorded.

3. RESULTS OF IMAGING AND REFLECTANCE SPECTROSCOPY

This chapter presents the results of SWIR imaging and VNIR-SWIR reflectance spectroscopy methods. It consists of two sections; section 3.1 describes the results from SWIR imaging spectroscopy, while section 3.2 provides the VNIR-SWIR reflectance spectroscopy results of the different rock components from the lithium-bearing pegmatite system. The classification system adopted in this study is based on the revised G1 – G5 granite classification type (Simons et al., 2016; 2017).

3.1. SWIR imaging spectroscopy results

The reflectance spectra of imaging spectroscopy based on the selected image pixels correspond to the coordinates in (Table 3.1, column 3) of each sample. These spectra contain distinct absorption features with similar mineralogy in each component of the system. Due to the size of the images from the datasets, few of the representative samples will be presented in this section while others can be found in Appendix III. This section is divided into four subsections based on the different components of the lithium-bearing pegmatite system: muscovite granite (G2), biotite granite (G3), topaz granite (G5a), and aplite pegmatite (G5b). All of the wavelength maps except for sample PEME4 were produced using automatic depth stretching in the wavelength range (2180-2225nm) to avoid losing details of the features.

To map the occurrence and absence of topaz in all the samples (Appendix IV and V) a depth stretching of 0-50% was applied in the wavelength range 2079-2086 nm to reveal the main absorption features from each pixel because automatic depth stretching does not consider pixels with shallow absorption features. The SWIR imaging spectroscopy results showed different patterns and pixels containing muscovite, illite, tourmaline, biotite, and topaz across the system. To determine the variation of the aluminous micas using the shift in the Al-OH and crystallinity values to show variation in the rock samples, and also show the presence of pixels containing zinnwaldite the decision tree classification (Appendix VII) was used to determine diagnostic features using the deepest absorption feature of the surface area of identified minerals, although the decision tree does not account for mixtures which could lead to missing out some of the end members (van Ruiteenbeek et al., 2019; Maghsoudi Moud et al., 2021; van Ruiteenbeek et al., 2014).

Table 3.1: The interpreted spectral parameters and mineralogy of selected reference spectra of rock samples from the different components of the system

Component	Sample ID	Coordinates (col, row)	Spectral mineral	OH feature (nm)	Deepest absorption feature		Second deepest absorption feature		Third deepest absorption feature		Crystallinity	
					Wavelength (nm)	depth	Wavelength (nm)	depth	Wavelength (nm)	depth		
batholith granite	BGCM	164,1207	muscovite	1408	2207	0.42	2366	0.45			4.05	muscovite (Al-rich)
		262,1217	illite	1411	2207	0.22	2359	0.22			3.43	illite (Al-poor)
		109, 1090	muscovite	1411	2207	0.26	2353	0.28			6.57	muscovite (Al-rich)
	BGCH	260,499	tourmaline	1408	2203	0.11	2366	0.16	2249	0.13	9.95	tourmaline
		285,617	muscovite	1409	2206	0.11	2353	0.11			5.12	muscovite (Al-rich)
		189, 573	illite	1409	2205	0.29					0.70	illite (Al-poor)
	BGFO	327,739	tourmaline		2203	0.08	2249	0.09	2366	0.06	8.17	tourmaline
		328,1644	tourmaline		2203	0.17	2246	0.20	2369	0.13	5.19	tourmaline
		354, 1749	illite	1411	2203	0.37					0.83	illite (Al-poor)
	BGME	262,861	tourmaline		2207	0.25	2239	0.29	2372	0.21	7.42	tourmaline
		323,650	tourmaline		2203	0.38	2242	0.43	2366	0.34	5.43	tourmaline

		329, 830	illite	1414	2210	0.52					0.41	illite
	BGHA	123,1680	tourmaline		2203	0.43	2246	0.46	2369	0.39	5.53	tourmaline
		324,1839	biotite		2252	0.13	2366	0.10			1.62	biotite
		127, 1546	illite	1409	2207	0.56	2357	0.53	2248	0.59	0.90	Illite (Al-poor)
topaz granite	TGNA4	135,948	topaz	1402	2083	0.18	2203	1.20	2366	0.18	2.06	topaz
		204,1150	illite + topaz	1418	2210	0.24	2346	0.23	2083	0.28	0.92	illite_topaz (Al-poor)
		110, 1137	illite + topaz	1411	2210	0.18	2083	0.35	2082	0.31	1.24	illite_topaz (Al-poor)
	TGNA5	80,1759	topaz	1402	2083	0.13	2203	0.15	2366	0.14	1.35	topaz
		90,1534	illite	1411	2210	0.23	2366	0.22			0.65	illite (Al-poor)
	TGNA6	216,622	topaz	1402	2083	0.24	2207	0.30	2340	0.27	2.50	topaz
		134,577	illite	1405	2197	0.17	2356	0.17			0.71	Illite (Al-poor)
	TGR1	380,1866	NH4 illite	1408	2203	0.44	2103	0.48	2002	0.49	1.05	NH4 illite (Al-poor)
		298,1904	illite	1398	2080	0.07	2203	0.15	2366	0.13	3.19	topaz_ muscovite (Al-poor)
		217, 1710	NH4 illite	1405	2203	0.20	2109	0.29	1996	0.31	0.97	NH4 illite (Al-poor)
	TGR2	215,1547	topaz	1402	2083	0.21	2203	0.36	2148	0.38	2.53	topaz
		262,1438	illite	1411	2207	0.23	2353	0.23			0.96	illite (Al-poor)
		278, 1413	Illite + topaz	1411	2207	0.33	2349	0.33	2080	0.37	0.84	topaz_ illite
	TGR3	259,951	topaz	1405	2086	0.40	2207	0.43	2385	0.41	1.01	topaz

		323,1033	tourmaline	1434	2203	0.22	2301	0.22	2369	0.18	2.50	tourmaline
		303, 1039	illite	1408	2203	0.34	2080	0.43			0.62	Illite (Al-poor)
	TGR4	254,617	topaz	1402	2080	0.12	2203	0.30	2372	0.25	2.85	topaz
		211,700	tourmaline	1411	2207	0.21	2297	0.22	2366	0.17	0.99	tourmaline
		306, 475	illite	1408	2203	0.52	2083	0.60			0.43	Illite (Al-poor)
aplite pegmatite	PEME1	289,1257	topaz	1402	2083	0.34	2207	0.40	2379	0.37	5.50	topaz
		95,1089	illite + topaz	1405	2210	0.46	2083	0.59	2388	0.46	1.77	illte_topaz (Al-poor)
		104,1238	tourmaline + topaz	1415	2203	0.28	2297	0.27	2372	0.22	3.95	tourmaline_topaz
		199,1226	muscovite_topaz	1382	2190	0.37	2372	0.32	2297	0.43	11.60	muscovite_topaz (Al-rich)
	PEME2	124,249	muscovite	1405	2194	0.14	2346	0.14			6.43	muscovite (Al-rich)
		281,1967	topaz	1405	2083	0.22	2207	0.30	2379	0.26	4.40	topaz
		74, 1826	illite + topaz	1405	2203	0.31	2083	0.35			1.24	illite_ topaz (Al-poor)
		126, 1774	tourmaline + topaz	1407	2203	0.25	2297	0.23	2249	0.27	4.53	tourmaline_topaz
	PEME3	150,790	muscovite	1405	2200	0.22	2362	0.18	2083	0.28	5.35	muscovite_topaz (Al-rich)
		294,704	topaz	1402	2083	0.231	2203	0.233	2362	0.24	5.79	topaz
		261, 573	illite	1405	2203	0.22					0.36	Illite (Al-poor)
		262, 433	tourmaline	1407	2203	0.26	2236	0.28	2359	0.23	4.53	tourmaline

3.1.1. Muscovite granite

The muscovite granite samples classified as G2 granite were obtained from Cligga Head and Carn Marth. They had fine-to-coarse-grained, microperthitic feldspar phenocrysts, Li siderophyllite with an abundance of muscovite mica and visually recognized crystals of quartz, plagioclase, and accessory minerals; tourmaline, topaz, apatite, zircon, rutile ilmenite and fluorite (Simons et al., 2016; 2017). As muscovite becomes dominant, the Li siderophyllite trends towards zinnwaldite and plagioclase near albite in terms of composition (Simon et al., 2017). The studied muscovite samples BGCH and BGCM have the deepest absorption features between approximately 2203 and 2207 nm (Table 3.1 column 6). The deepest absorption features of the interpreted minerals are due to the Al-OH bonds in muscovite, illite, and the B-OH bonds in tourmaline (Clark et al., 1990). In sample BGCH, the wavelength map (Fig. 3.1a) predominantly shows greenish pixels with high brightness values above 4 in the illite-muscovite crystallinity (Table 3.1 column 12) indicating pixels containing muscovite, yellowish pixels with crystallinity values less than 4 indicate the presence of illite and whitish pixels indicate the presence of tourmaline (Fig. 3.1b).
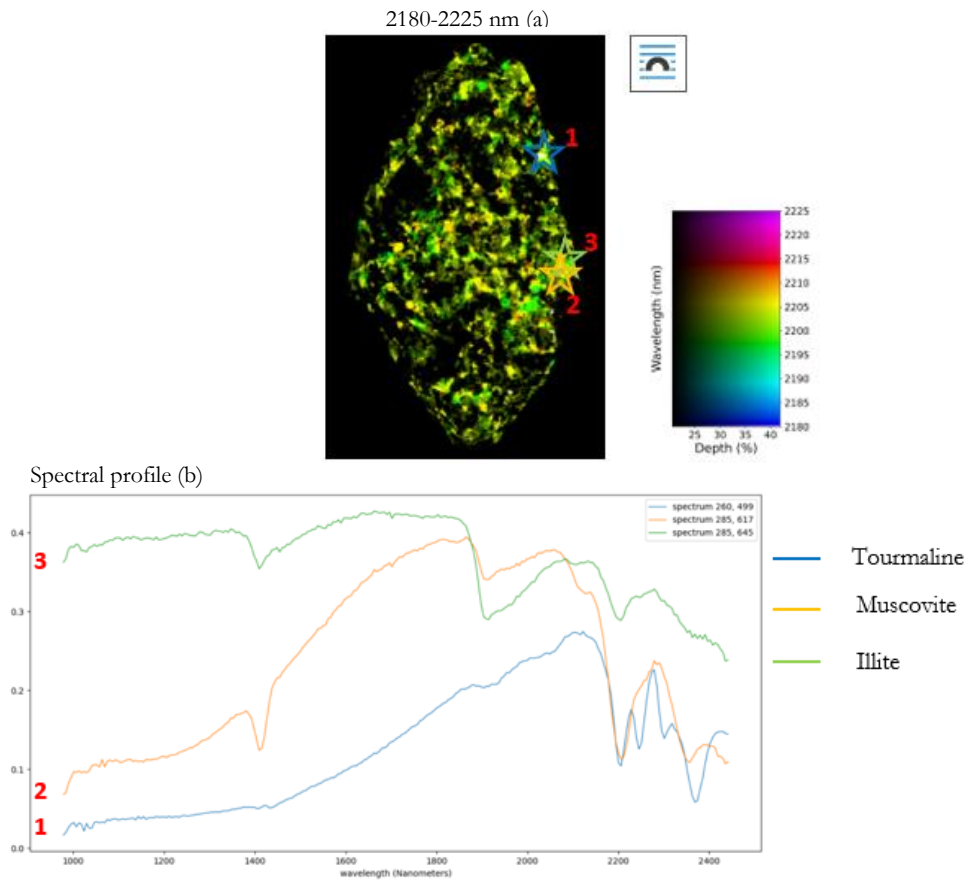

Figure 3.1: Wavelength map (a) of sample BGCH and (b) the spectral curve from the selected pixels

The absorption features around 1408-1409nm and 1901-1910nm indicate the presence of OH and water molecules in the sample. The black pixels in the wavelength map indicate the presence of very shallow or absence of absorption features between 2100 and 2400 nm indicating the presence of quartz and unaltered feldspars (Hecker et al. 2019c).

In the sample BGCM, there are predominant yellow to orange-colored pixels (Fig. 3.2a) with crystallinity values above 4 showing the presence of muscovite with low crystallinity values indicating the presence of illite (Fig. 3.2b). The absorption features at around 1408-1411nm and 1905-1908nm indicate the presence of OH and water molecules in the sample.
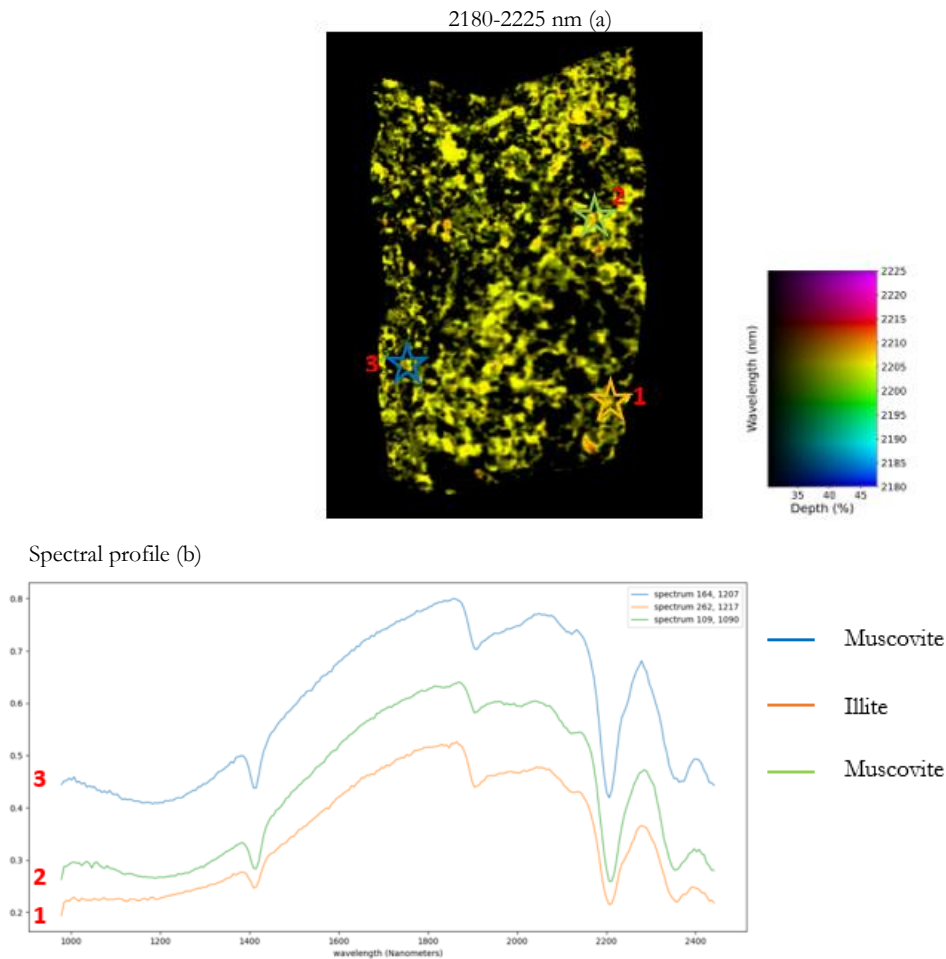

Figure 3.2: Wavelength map (a) of sample BGCM and (b) the spectral curve from the selected pixels

3.1.2. Biotite granite

The biotite granite samples classified as G3 granites were obtained from Foggintor quarry, Merrivale, and Harford. They had medium-to-coarse-grained, microperthitic feldspar phenocrysts, plagioclase, biotite, and accessory minerals; tourmaline, cordierite, monazite, zircon, apatite, ilmenite, and rutile (Simons et al., 2016). The studied biotite samples BGFO, BGME, and BGHA have the deepest absorption features between approximately 2203 and 2210nm (Table 3.1). The interpreted minerals have the deepest absorption features due to Al-OH bonds in illite, B-OH bonds related to tourmaline, and Mg-OH bonds in the BGFO and BGHA samples due to biotite (Clark et al., 1990).

In the sample BGFO, the wavelength map shows predominant light green (Fig.3.3a) in color with low crystallinity values and patches of whitish pixels indicating the presence of tourmaline (Fig.3.3b) and biotite. The absorption features at around 1411nm and 1904-1908nm indicate the presence of OH and water molecules in the sample. To identify the pixels containing biotite (Appendix VII), a wavelength length in the range of 2250-2260nm was created and shows blue-colored pixels indicating the presence of biotite.
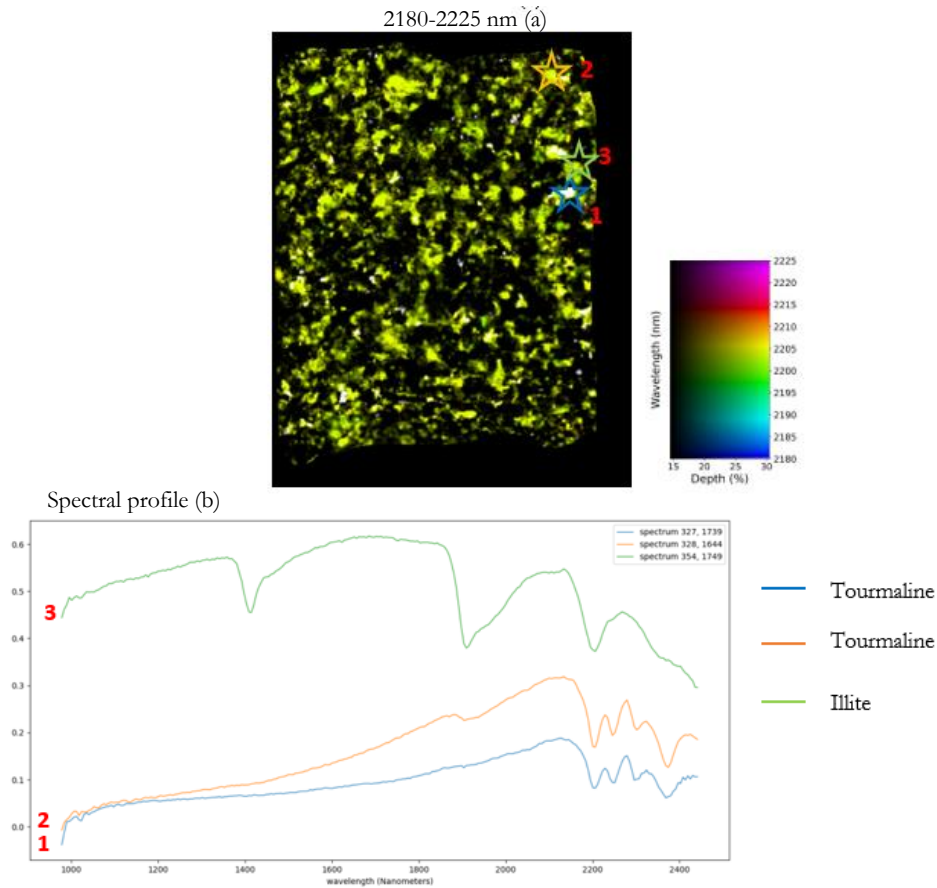

Figure 3.3: Wavelength map (a) of sample BGFO and (b) the spectral curve from the selected pixelss

In the sample BGHA, the wavelength map (Fig. 3.4a) shows variation in green colors with low crystallinity values indicating the presence of illite with white patches pixels showing the occurrence of tourmaline (Fig. 3.4b). The reddish pixels indicate the presence of illite at the longer wavelengths. The absorption features at around 1409nm and 1908nm indicate the presence of OH and water molecules in the sample.
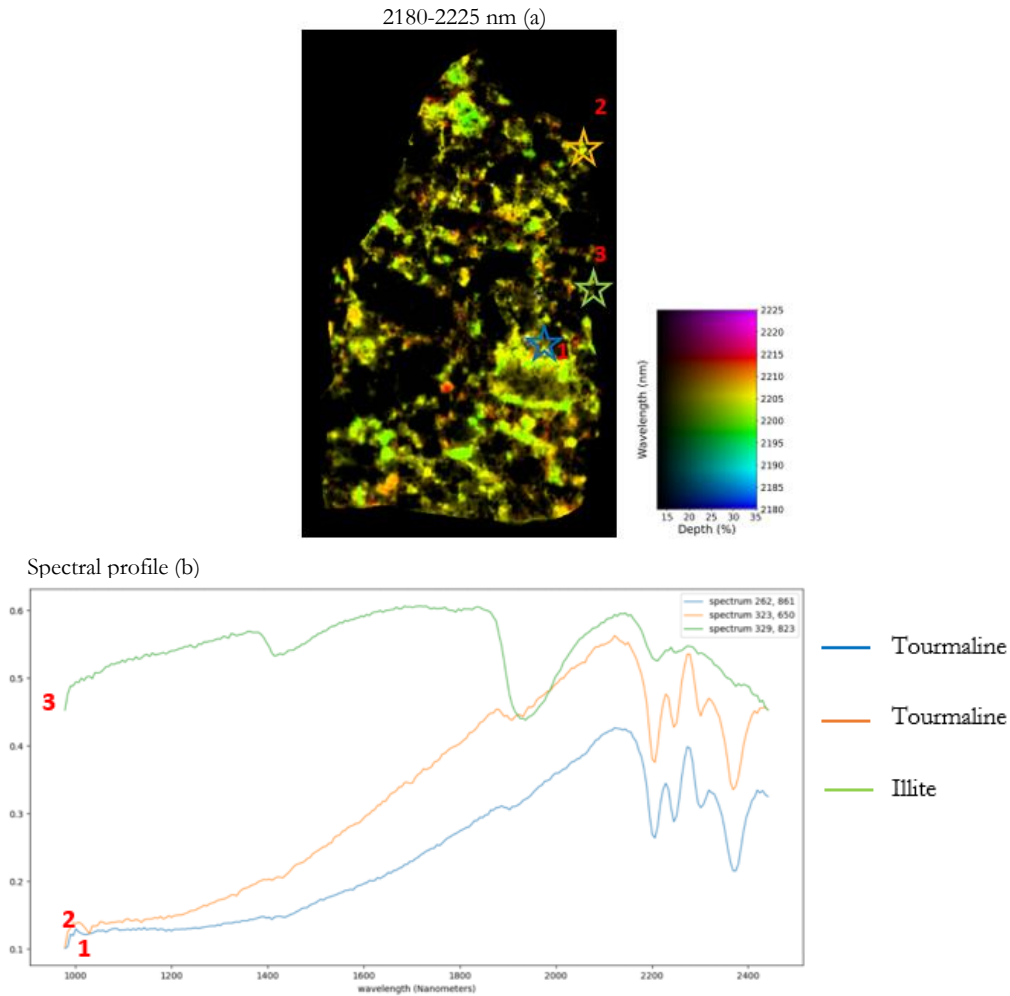

Figure 3.4: Wavelength map (a) of sample BGHA and (b) the spectral curve from the selected pixels

As observed in Fig. 3.5a, the scatterplot of the wavelength of the deepest absorption feature (aluminous micas) against the depth of the absorption feature shows a positive correlation, an indication of the shift of absorption features to longer wavelengths with increasing depth reflecting changes in alteration phases. In this study, this relation provides useful information about the variation in the wavelength shift in aluminous micas. On the other hand, a negative correlation (Fig. 35b) observed in the scatterplot of the deepest absorption feature with crystallinity indicates that the features decrease in wavelength with a decrease in crystallinity values.
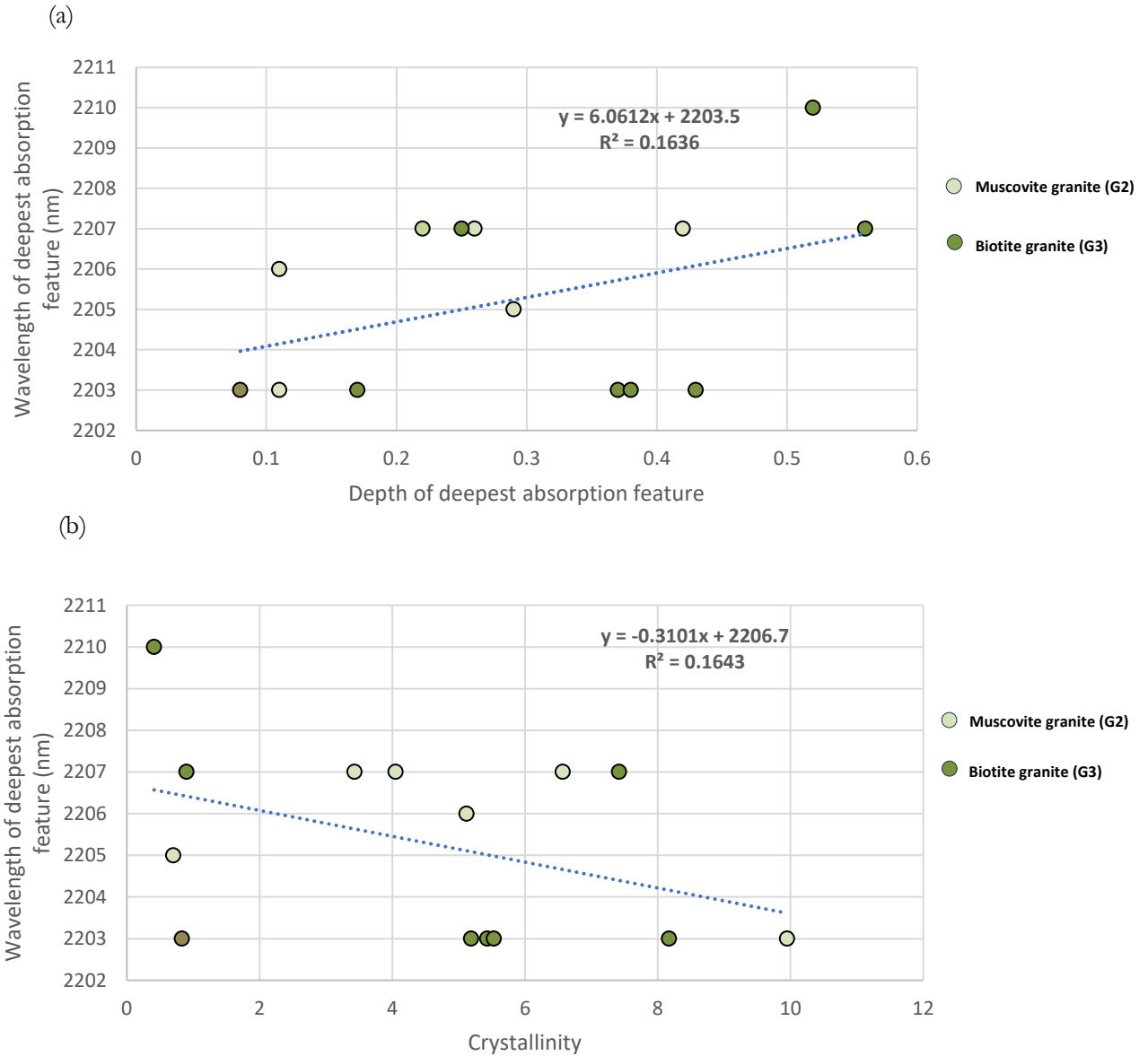
(a)

(b)

Figure 3.5: Relation between the wavelength of the deepest absorption feature of the aluminous micas and depth (a) and the wavelength of the deepest absorption feature with crystallinity values (b) in the selected pixels of muscovite and biotite granite samples to show a shift of wavelength position of the absorption feature.

3.1.3. Topaz granite

The topaz granite samples classified as G5a granites were obtained from Nanpean and Rinsey Cove and are medium-grained, comprising topaz, Li-Fe trioctahedral micas; zinnwaldite, and lepidolite with accessory minerals apatite, amblygonite, zircon, rutile, ilmenite, columbite-tantalite and cassiterite. The topaz granites

are formed from fluid-flux melting from a biotite-rich source and are not petrogenically linked to muscovite and biotite granites (Simons et al., 2017). The wavelength maps of the studied samples TGNA4, TGNA5, TGNA6 (from Nanpean) and TGR1, TGR2, TGR3, and TGR4 (from Rinsey Cove) show greenish to orange color with white pixels (Fig. 3.6a) indicating the presence of tourmaline and topaz (Appendix II). In sample TGNA4, the wavelength map appears orange in color with low crystallinity values indicating the presence of illite with a peak at 2083nm showing as topaz and a mixture of illite + topaz (Fig. 3.6b). To map topaz in all the samples, the wavelength map in 2079-2086 nm was created (Appendix III) to determine pixels with the occurrence of topaz.
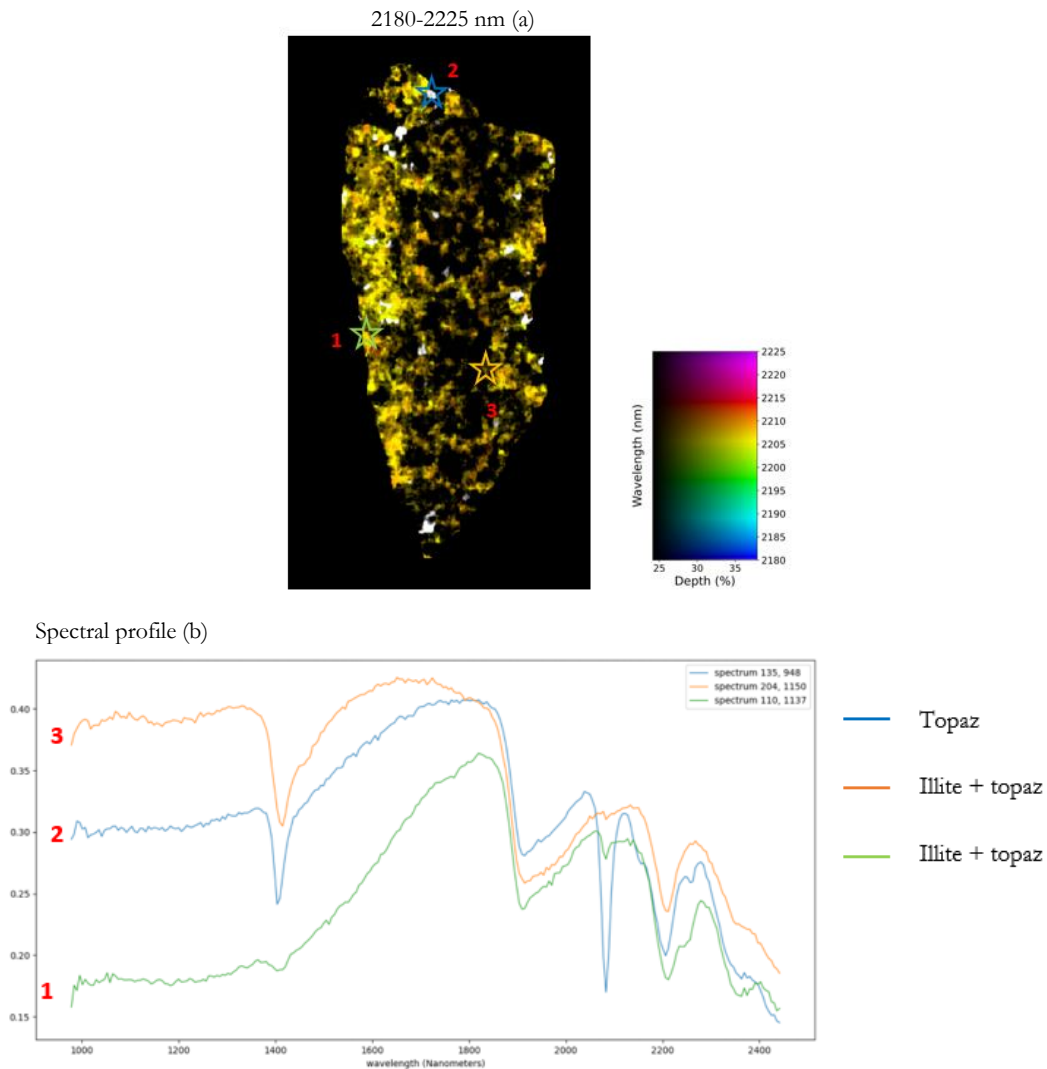

Figure 3.6: Wavelength map (a) of sample TGR1 and (b) the spectral curve from the selected pixelsw

As observed in Fig. 3.7a, the scatterplot of the wavelength of the deepest absorption feature (aluminous micas) against the depth of the absorption shows a negative correlation an indication of a shift in the feature as the wavelength decreases with depth. A scatterplot of the deepest absorption feature and crystallinity, however, showed no correlation (Fig. 3.7b), indicating their wavelength is independent of crystallinity.
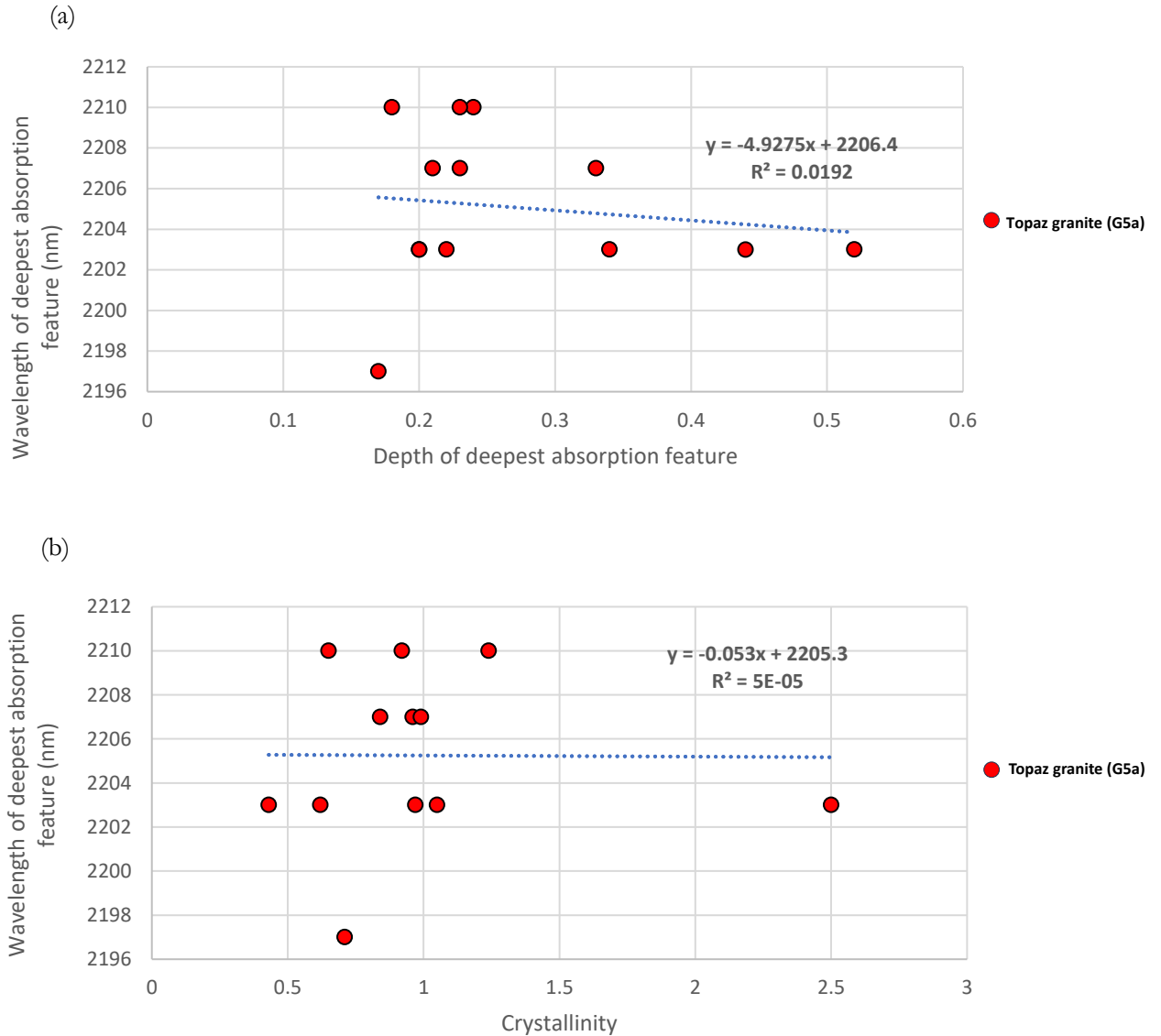

Figure 3.7: Relation between the wavelength of the deepest absorption feature of the aluminous micas and depth (a) and the wavelength of the deepest absorption feature with crystallinity values (b) in the selected pixels of topaz granite samples to show a shift of wavelength position of the absorption feature.

3.1.4. Aplite Pegmatite

The pegmatite sample classified as G5b granite obtained from Meldon is a topaz-rich aplite occurring in a metasedimentary host rock and is associated with accessory minerals; apatite, amblygonite, zircon, rutile, ilmenite, columbite-tantalite and cassiterite (Simons et al., 2017). The studied samples PEME1, PEME2, and PEME2 show variation in color from green to yellow indicating the presence of muscovite, illite, tourmaline, topaz, and pixels comprising muscovite + topaz, tourmaline + topaz, and illite + topaz. In sample PEME1, the wavelength map (3.8a) shows a green to yellowish color indicating the presence of different mixtures of muscovite, illite, and tourmaline with topaz (3.8b).
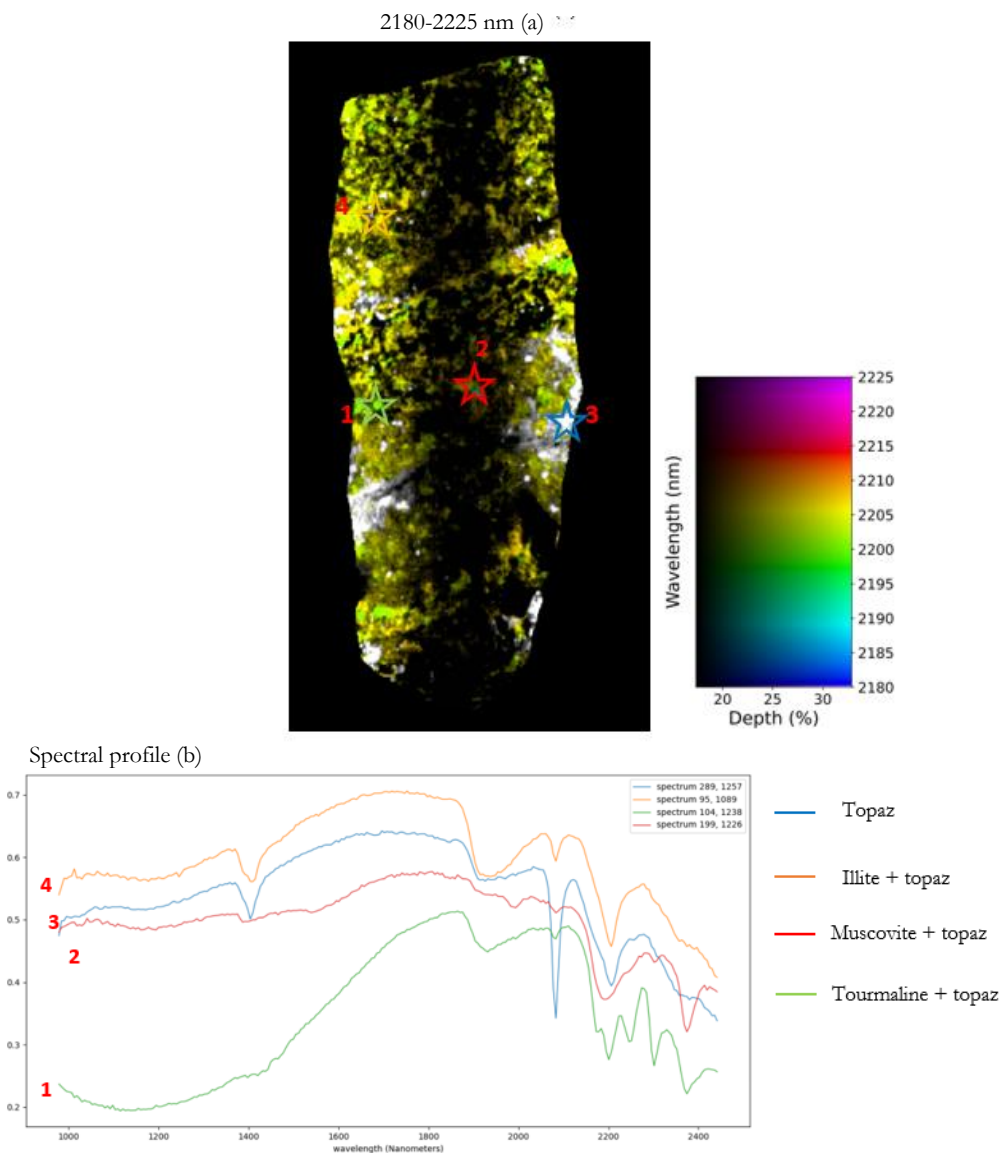

Figure 3.8: Wavelength map (a) of sample PEME1 and (b) the spectral curve from the selected pixels

As observed in Fig. 3.8a, the vertical band running through the center of the wavelength map is attributed to the cooling of the camera. The scatterplot of the wavelength of the deepest absorption feature (aluminous micas) against the depth of the absorption (Fig. 3.9a) shows a positive correlation and an indication of a shift in the feature as the wavelength increases with depth. On the other hand, a negative correlation (Fig. 3.9b) observed in the scatterplot of the deepest absorption feature with crystallinity indicates that the features decrease in wavelength with a decrease in crystallinity values.

(a)

(b)

Figure 3.9: Relation between the wavelength of the deepest absorption feature of the aluminous micas and depth (a) and the wavelength of the deepest absorption feature with crystallinity values (b) in the selected pixels of aplite pegmatite samples to show a shift of wavelength position of the absorption feature.

In all the studied samples, a positive correlation can be observed in the scatterplot of the wavelength of the deepest absorption features against depth (Fig. 3.10a) and a negative correlation in the scatterplot of the wavelength of the deepest absorption feature against crystallinity (Fig. 3.10b) to show variations in the wavelength absorption features indicating magmatic fractionation where different minerals are formed by depth.
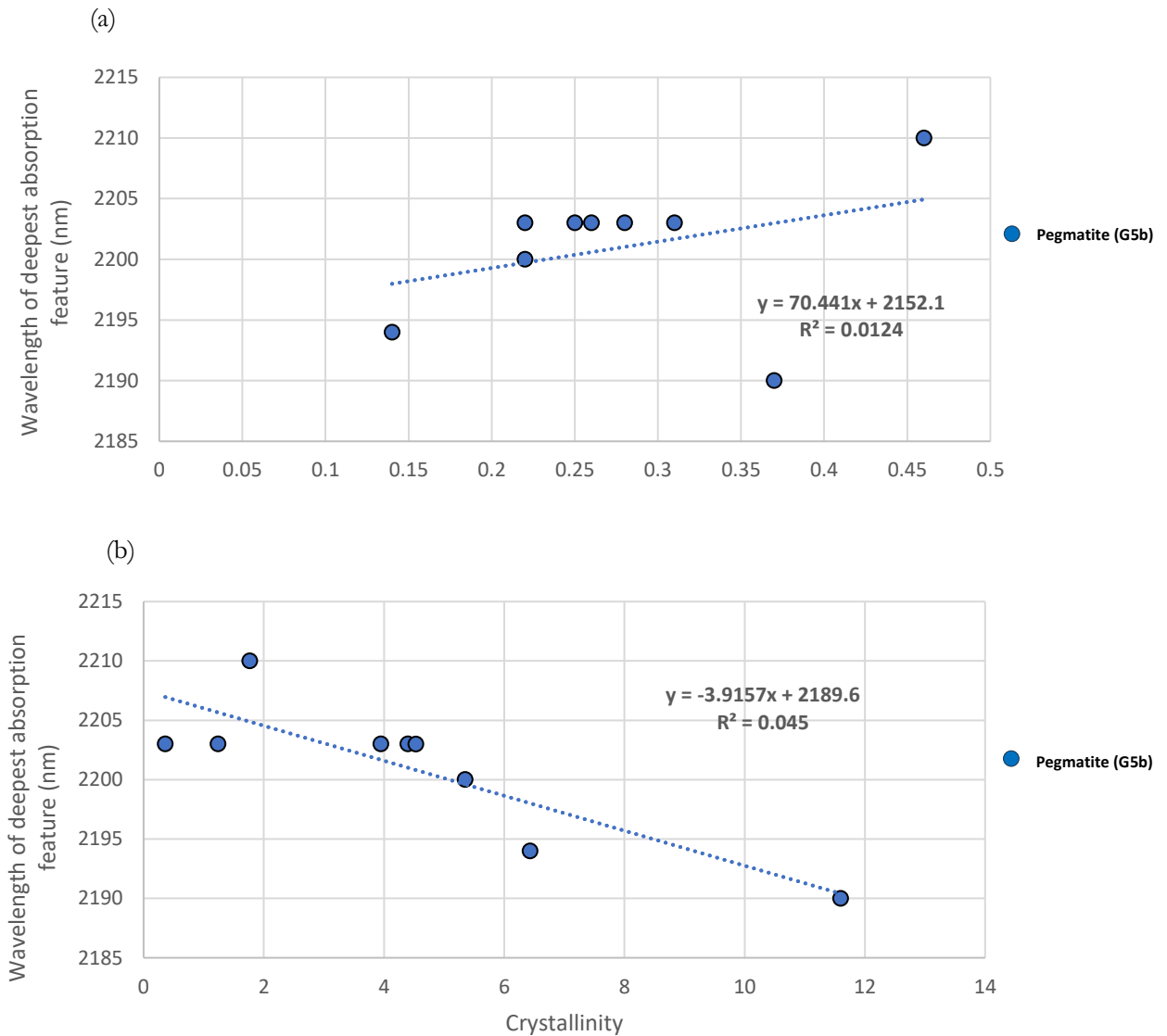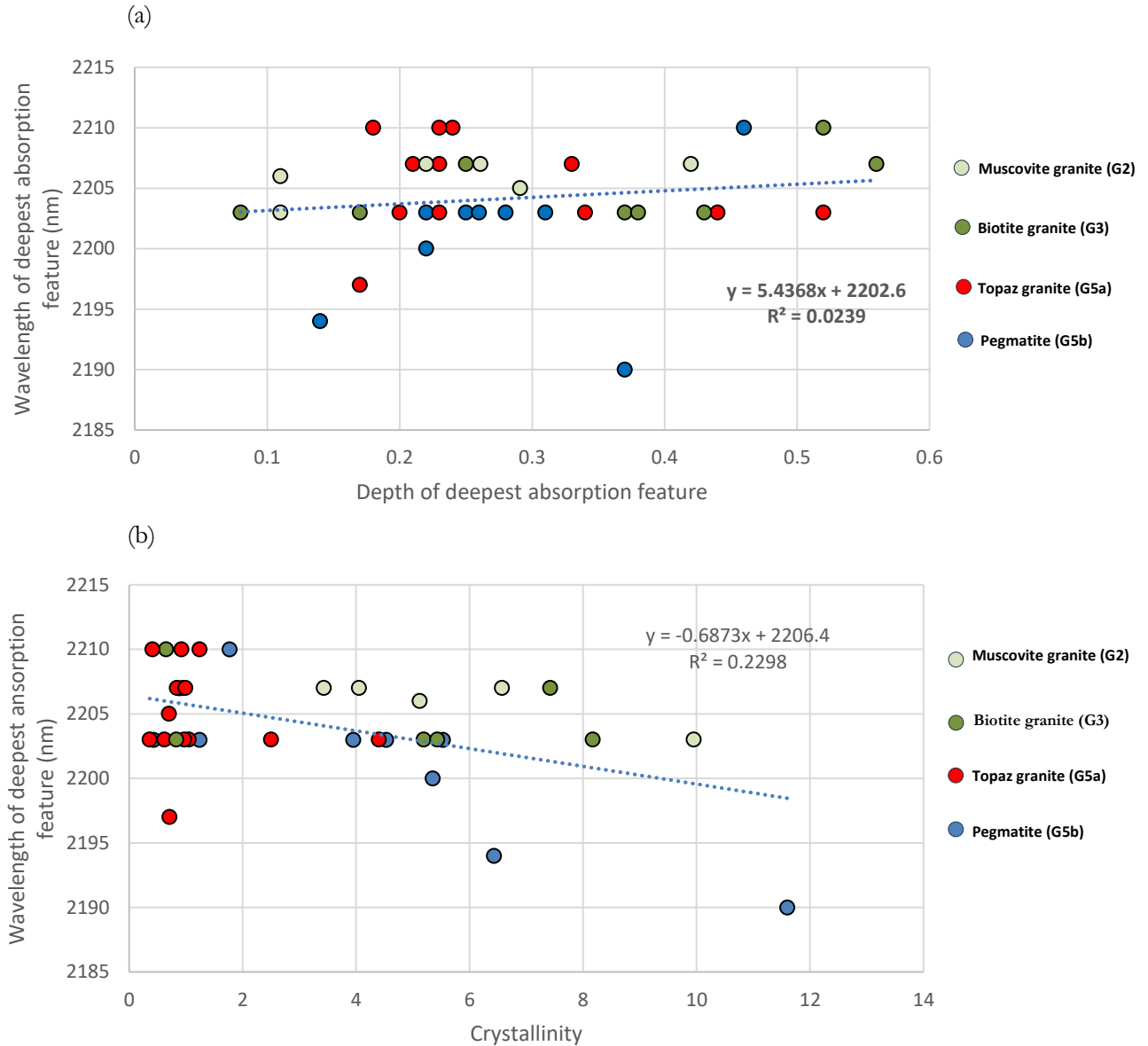
(a)

(b)

Figure 3.10: Relation between the wavelength of the deepest absorption feature of the aluminous micas and depth (a) and the wavelength of the deepest absorption feature with crystallinity values (b) in all the studied samples to show a shift of wavelength position of the absorption feature.

3.2. VNIR-SWIR reflectance spectroscopy

This section presents the VNIR-SWIR reflectance spectroscopy results of the spectral characteristics in the wavelength range of 350– 2500 nm. The section provides the VNIR-SWIR wavelength ranges of the spectral characteristics of rock types in the different components of the system. The stacked spectra (Fig. 3.11) provide an understanding of the trend during the fractionation process from the batholith granites to the aplite pegmatite. A summary of the band assignments and interpreted minerals can be found in Table 3.2.
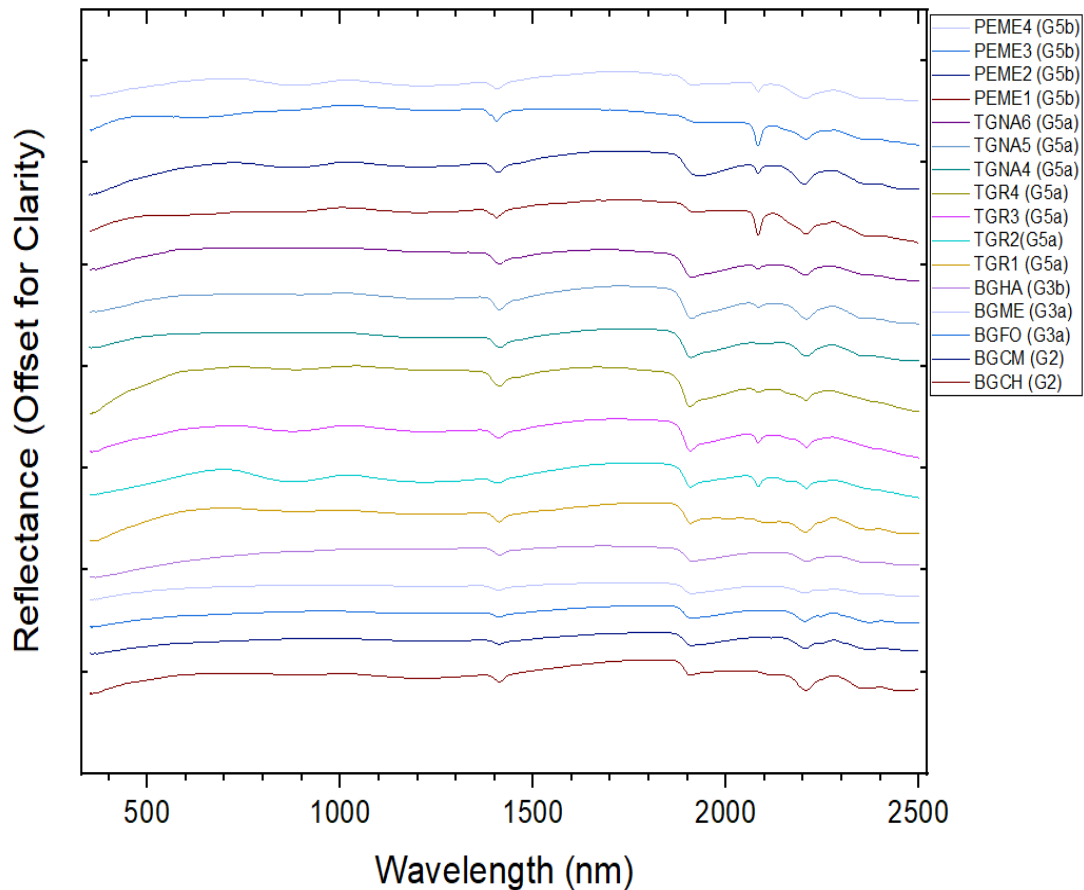
Figure 3.11: Stacked reflectance spectra of all the studied samples. The samples are stacked based on the type level (G2-G5b). G2 are the muscovite granites; G3a and G3b are the biotite granites; G5a are the topaz granites; and G5b are the aplite pegmatites.

3.2.1. Muscovite granite

The studied muscovite granite samples BGCH and BGCM show distinct absorption features in the VNIR-SWIR wavelength range (Fig. 3.12a). Spectral zoom to the 2100-2400 nm range (Fig.3.12b) shows both samples display the deepest absorption features due to the Al-OH vibration bond at 2204-2206 nm and a

second absorption feature at wavelength range 2351-2372 nm due to an overtone from Al-OH indicating the presence of muscovite. The third absorption feature in sample BGCH at 2247nm due to Fe-OH could be attributed to the presence of biotite. In the VNIR spectrum range (400 – 1300nm), the absorption feature around 900 and 1200 nm indicate the presence of Fe, with the features at 1906-1908 nm and 1409-1411 nm indicating water molecules and OH in the samples (Clerk et al., 1990).
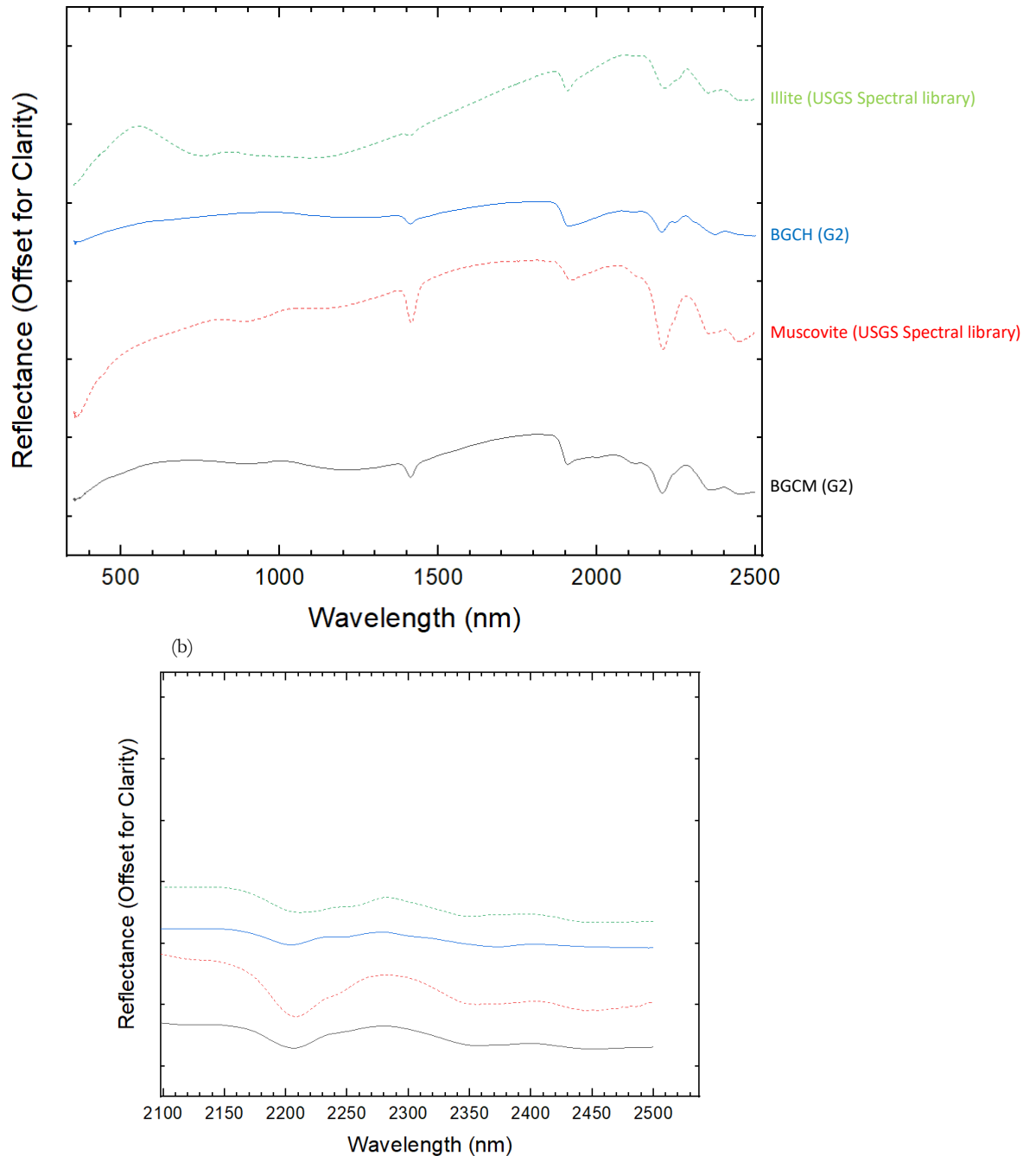
(a)

(b)

Figure 3.12: The reflectance spectra (a) and a spectral zoom (b) in the 2100-2500 nm range of muscovite granite (G2) sample

3.2.2. Biotite granite

The studied biotite granite samples (BGFO, BGME, and BGHA) show distinct absorption features in the VNIR-SWIR wavelength range (3.13a). A spectral zoom in the 2100-2400 nm range (3.13b) shows the absorption feature at 2204-2011 nm due to the Al-OH vibration bond and a second absorption feature at 2353-2369 nm due to the Mg-OH indicating the presence of muscovite. The diagnostic absorption features at 2248-2250 nm could be due to Fe-OH indicating the presence of biotite.
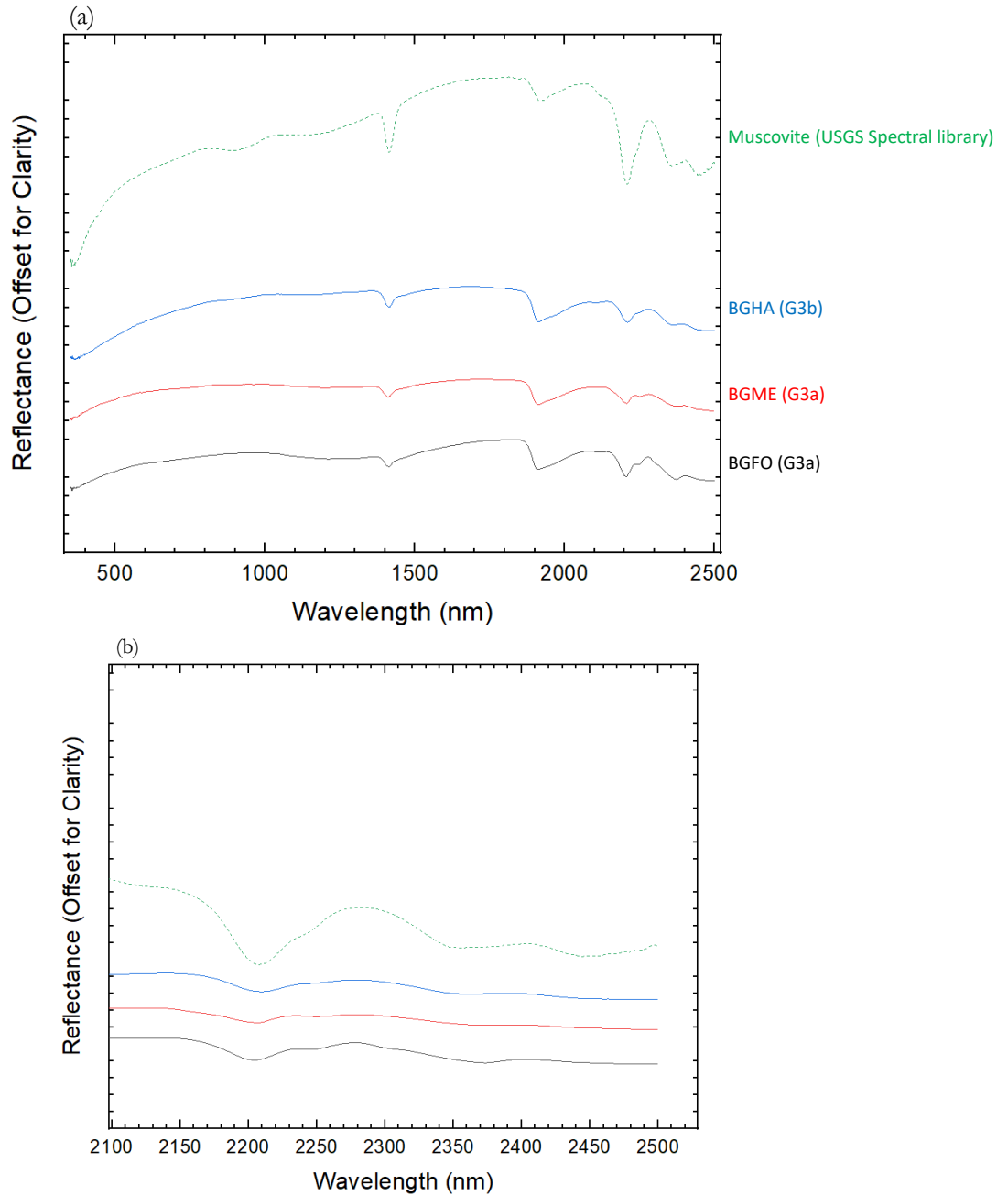
Figure 3.13: The reflectance spectra (a) and a spectral zoom (b) in the 2100-2500 nm range of biotite granite sample

3.2.3. Topaz granite

The VNIR-SWIR range (Fig.3.14a). The spectral zoom to the SWIR wavelength range shows distinct absorption features at approximately 2208-2210 nm due to the Al-OH bonds and a second deepest feature at 2350-2353 nm due to the Mg-OH indicating the presence of muscovite in all the samples except sample TGR1 which shows a second deepest feature at 2342 nm, doublet at 2000 nm and 2100 nm indicating the presence of NH4 illite (Fig. 3.14b).

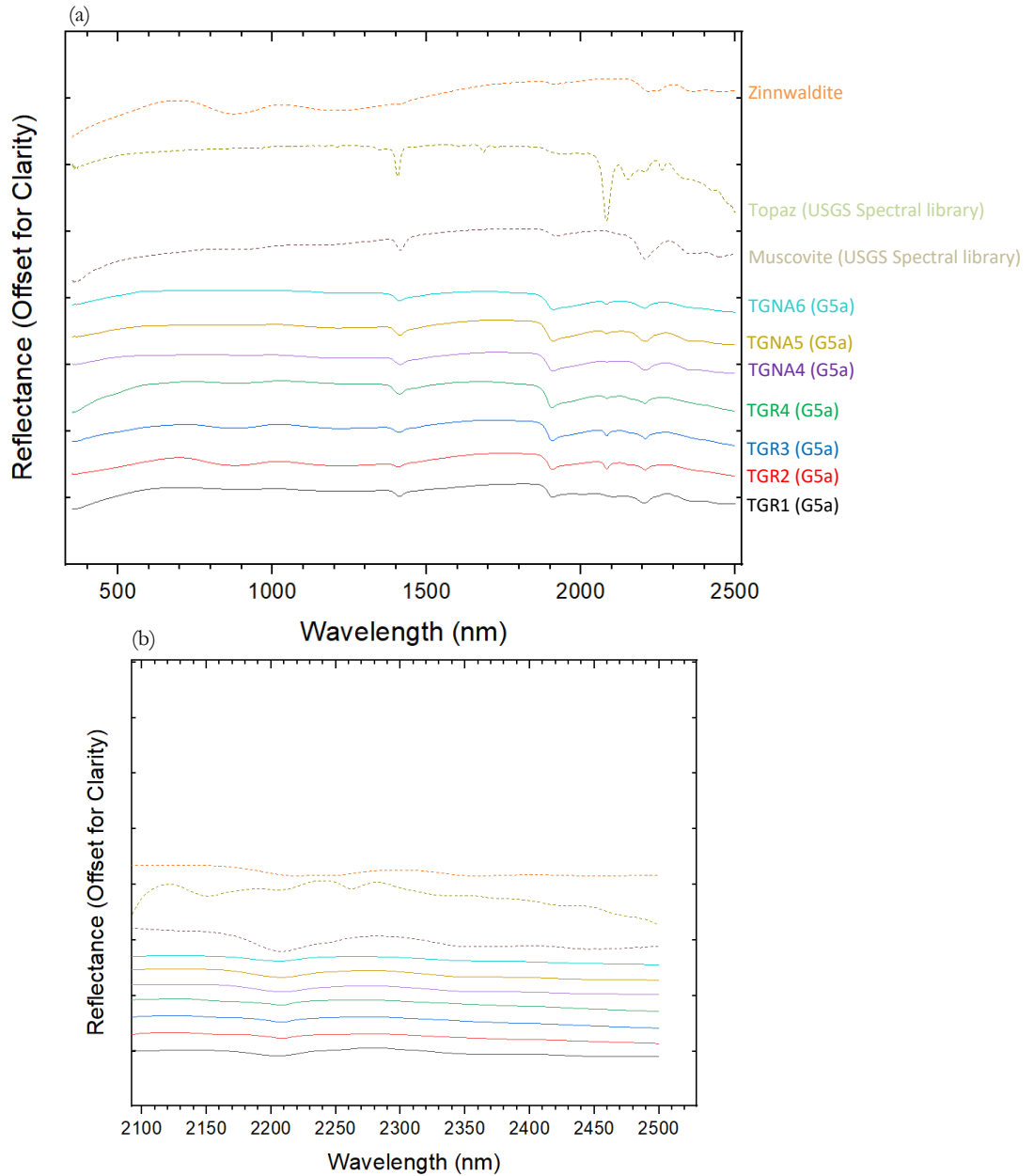

Figure 3.14: The reflectance spectra (a) and a spectral zoom (b) in the 2100-2500 nm range of the topaz granite (G5a) samples

The feature at 2083 nm indicates the presence of topaz in all samples except for sample TGR1. All the studied samples show the absorption feature in 1405-1410 nm due to the presence of the OH absorption band and further absorption feature at approximately 1900nm due to water molecules in the samples (Clerk et al., 1990). In the VNIR range of the spectrum, except for sample TGR1, all other samples display distinct absorption features close to 870-880 nm and 1215-1222 nm due to Fe indicating the presence of zinnwaldite.

3.2.4. Aplite Pegmatite

The studied aplite pegmatite samples show distinct absorption in the VNIR-SWIR range of the spectrum (Fig. 3.15a). A spectral zoom at the SWIR range indicates an absorption feature at the wavelength range 2205-2208 nm due to the Al-OH vibration bond and further displays a second absorption feature due to Mg-OH at the wavelength range 2351-2353 nm indicating the presence of muscovite in all samples with a third absorption feature in sample PEME3 at 2262 nm due to Fe-OH (Fig. 3.15b). The feature at 2083 nm shows the presence of topaz in all the samples. In the VNIR range of the spectrum, the samples exhibit distinct absorption features at around 880 nm and 1200 nm due to the Fe indicating the presence of zinnwaldite in samples PEME1, PEME2, and PEME4 except for sample PEME3 which has an absorption feature at around 580 nm due to the presence of lepidolite.
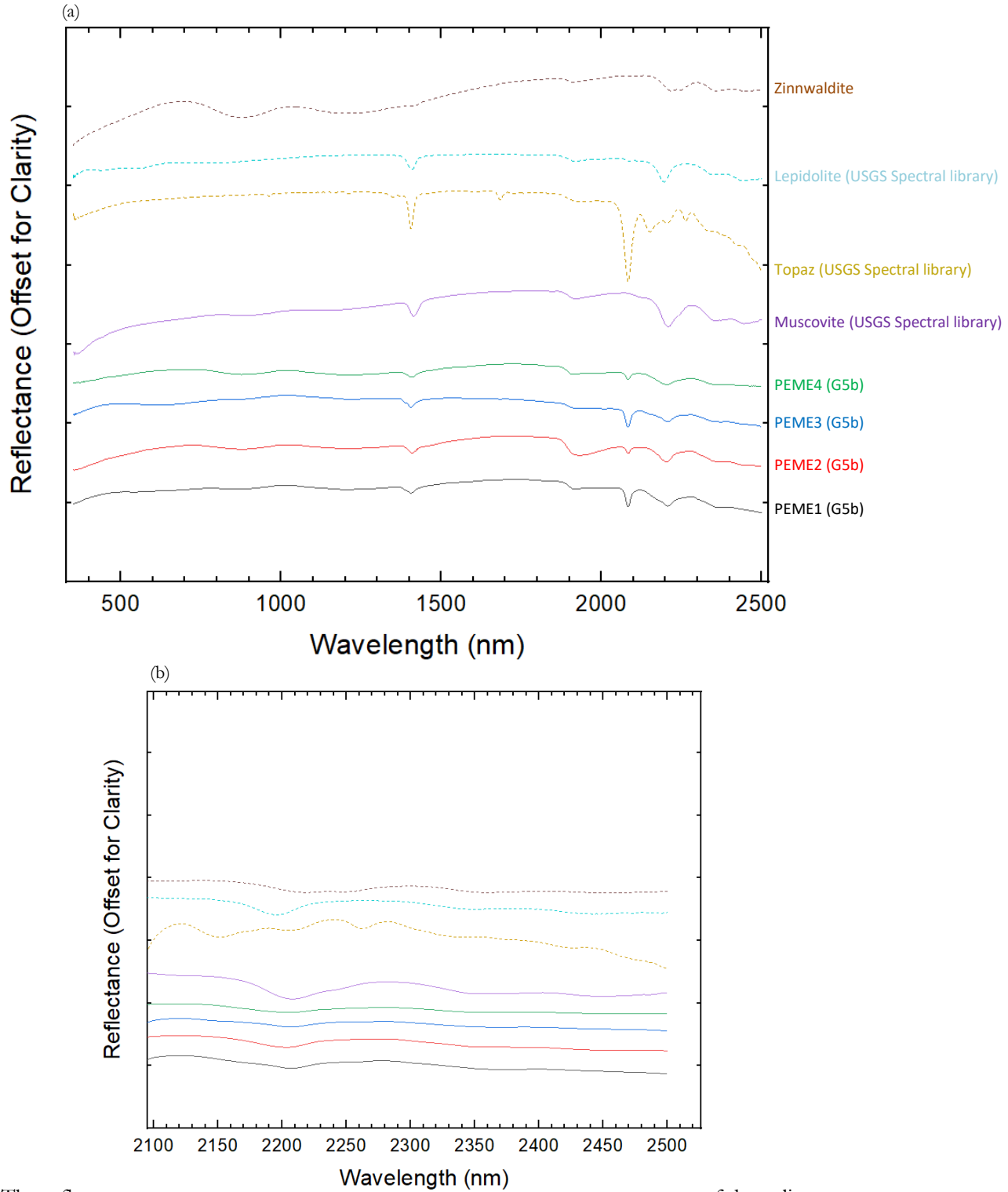
Figure 3.15: The reflectance spectra (a) and a spectral zoom (b) in the 2100-2500 nm range of the aplite pegmatite (G5b) samples

Table 3.2: Band assignment and interpreted minerals from the studied samples

|	Sample ID	Bulk Spectrum mineral	OH + H$_2$O feature (nm)	H$_2$O feature (nm)	VNIR spectrum absorption features	SWIR spectrum absorption features		
						First deepest feature (nm)	Second deepest feature (nm)	Secondary Al-OH feature (nm)
Cations					**Fe**	**Al-OH**	**Fe-OH**	
Batholith granite	BGCH	muscovite	1414	1908	1210	2209	2247	2351
	BGCM	muscovite	1409	1906	902/1200	2202		2372
	BGME	muscovite	1414	1906	1205	2201	2249	2377
	BGFO	muscovite	1411	1909	1208	2207	2250	2373
	BGHA	muscovite	1412	1908		2208		2358
Cations					**Fe**	**Al-OH**	**Al-OH**	
Topaz granite	TGNA6	muscovite, topaz,	1408	1910		2209	2082	2349
	TGNA5	muscovite, topaz	1412	1906		2207	2082	2344
	TGNA4	muscovite, topaz	1411	1903		2210	2084	2347
	TGR4	muscovite, topaz, zinnwaldite	1409	1904	871, 1222	2207	2084	2354
	TGR3	muscovite, topaz, zinnwaldite	1413	1906	871, 1218	2208	2081	2368
	TGR2	muscovite, topaz, zinnwaldite	1410	1909	880, 1215	2209	2084	2363
	TGR1	NH4 illite, topaz	1412	1907		2205	2084	2353
Cations					**Fe or Mn**	**Al-OH**	**Al-OH**	
Pegmatite	PEME4	muscovite, topaz, zinnwaldite	1410	1906	887, 1209	2205	2084	2347
	PEME3	muscovite, topaz, zinnwaldite	1405	1910	574, 883, 1207	2208	2084	2347
	PEME2	muscovite, topaz, zinnwaldite, lepidolite	1412	1921	877, 1204	2202	2085	2354
	PEME1	muscovite, topaz, zinnwaldite	1404	1914	861, 1214	2209	2081	2357

Note: Band assignment of cations of the studied samples (adopted from Clark et al.,1990; Cardoso-Fernandes et al., 2021; Mekonnen, 2023)

4. RESULTS OF XRD, XRF AND MAGNETIC SUSCEPTIBILITY

This chapter presents the results of the XRD and XRF analysis of the studied rock samples to determine the typical mineralogy of the rock types in the lithium-bearing pegmatite system. It is divided into two parts; section 4.1 provides the result of the XRD to determine the mineral composition and section 4.2 the XRF result to compare the concentrations of potassium, thorium, and uranium with the airborne radiometric signatures.

4.1. Results of XRD

The XRD diffractogram of the studied samples is stacked based on the type-level classification (Simons et al., 2017) of the different rock types in the lithium-bearing pegmatite system (Fig. 4.1a). The patterns showed quartz as a sharp peak and dominant at approximately 21°, 27°, 37°, 40°, 50°, and 55° 2θ in all the samples. Albite had prominent peaks at 14°, 22° and 28° 2θ. A zoom into the peak range 5°-35° 2θ (Fig.4.1b) shows additional peaks at approximately 18° and 46° 2θ (Fig.4.1a) indicating the presence of muscovite/illite in all the samples. Similar patterns can be observed with peaks at approximately 22° and 35°2θ indicating the presence of schorl (black tourmaline) in all the studied samples. The peaks at 24°, 26°, 28° and 31° 2θ show the presence of topaz in all the studied samples. In the batholith granite samples (Fig.4.1c, red color) similar peaks at 8°-9° 2θ could be due to the presence of biotite and/or muscovite/illite. The XRD diffractogram analysis from the batholith granite to the pegmatite shows a trend associated with increasing magmatic differentiation and reflects the changes in mineral phases as the magma evolves. This can be observed as the muscovite/illite peak at 18° 2θ becomes more prevalent in the pegmatite and the shift of the biotite peak at 8-9° 2θ in the batholith granite to muscovite/illite/zinnwaldite or lepidolite is an indication of a change in the chemical environments from the batholith granites to the pegmatites.

(a)

(b)
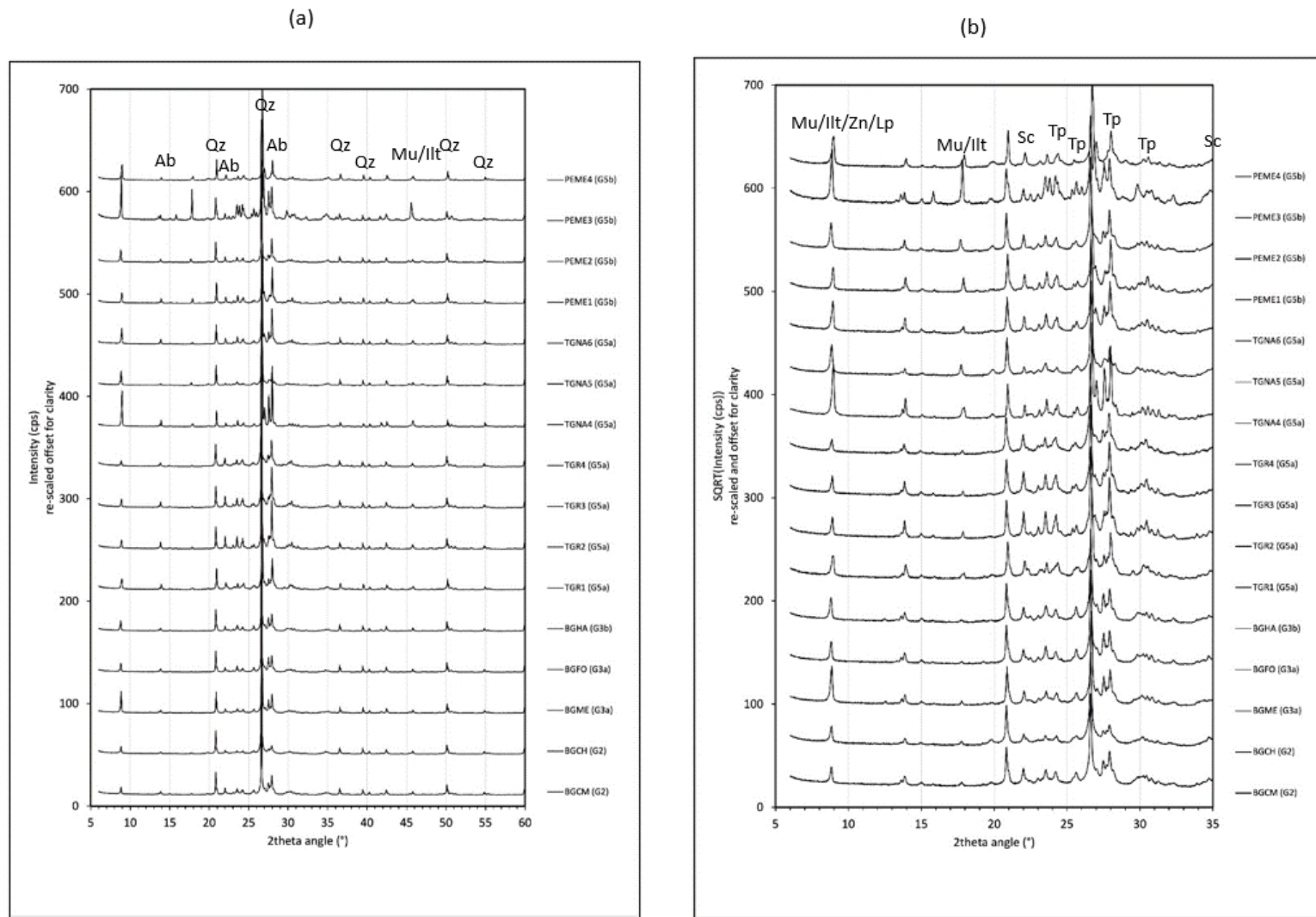
Abbreviations: Qz-Quartz   Ab-Albite   Mu-Muscovite   Ilt-Illite   Sc-Schorl   Tp-Topaz   Zn-Zinnwaldite   Bi-Biotite   Lp-Lepidolite
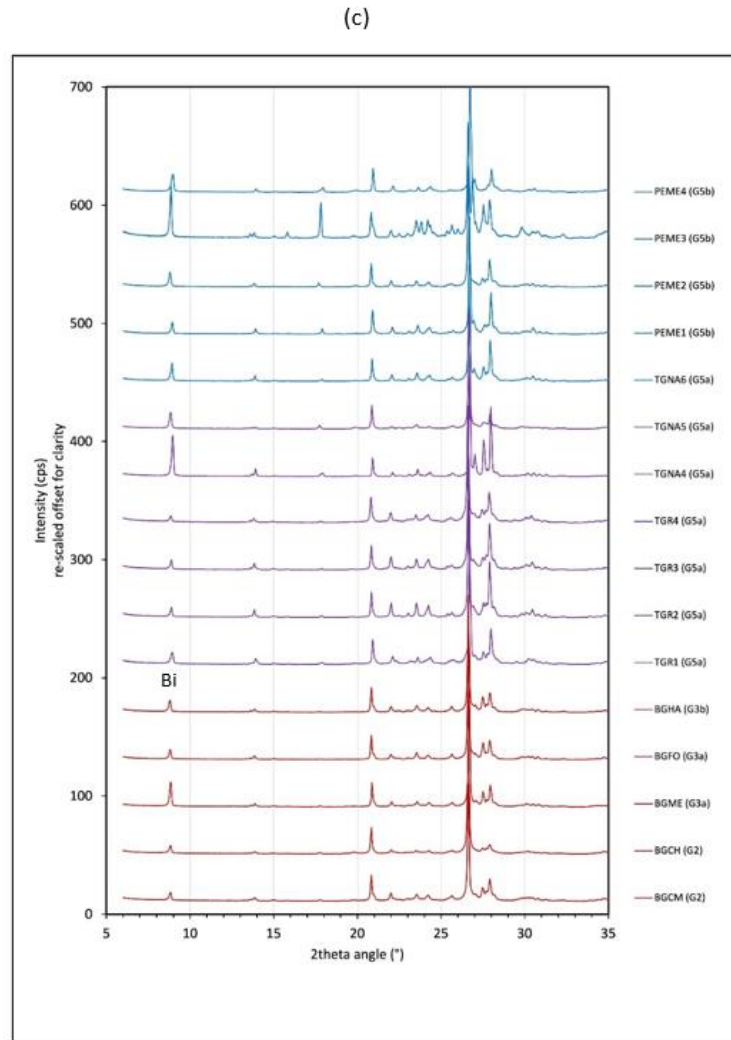
Figure 4.1: XRD patterns of the studied rock samples. All samples show similar diffraction peaks in the 5-60° 2ϴ range (a). An extra offset square root intensity and 0 to 35° on the 2ϴ to emphasize the low-intensity peaks since not much difference can be observed in the diffraction patterns after 35° (b). Figure (c) shows an offset intensity and 0 to 35° on the 2ϴ between the different groups of samples, red for batholith granite, purple topaz granite, and blue pegmatites.

4.2.   Results of XRF

The XRF results in this study consider the concentrations of potassium, thorium, and uranium to guide the interpretation of the airborne radiometric dataset. Potassium is typically associated with k-feldspars and mica minerals and areas with high potassium concentrations can indicate the presence of such minerals. Fig.4.2a shows all the studied samples to have 1-3.38 % potassium concentration indicating the presence of k-feldspars and mica minerals. A fairly high thorium concentration value (Fig. 4.2b) in the muscovite and biotite granites indicates the presence of thorium-rich monazite (Simons et al., 2017). Similarly, the uranium concentration can indicate the presence of uranium-rich accessory minerals such as zircon (Simons et al., 2016, 2017). The high (100-237 ppm) concentration of uranium (Fig.4.2c) could indicate an accuracy issue with the pXRF and will be compared with data from Simons et al., 2017.
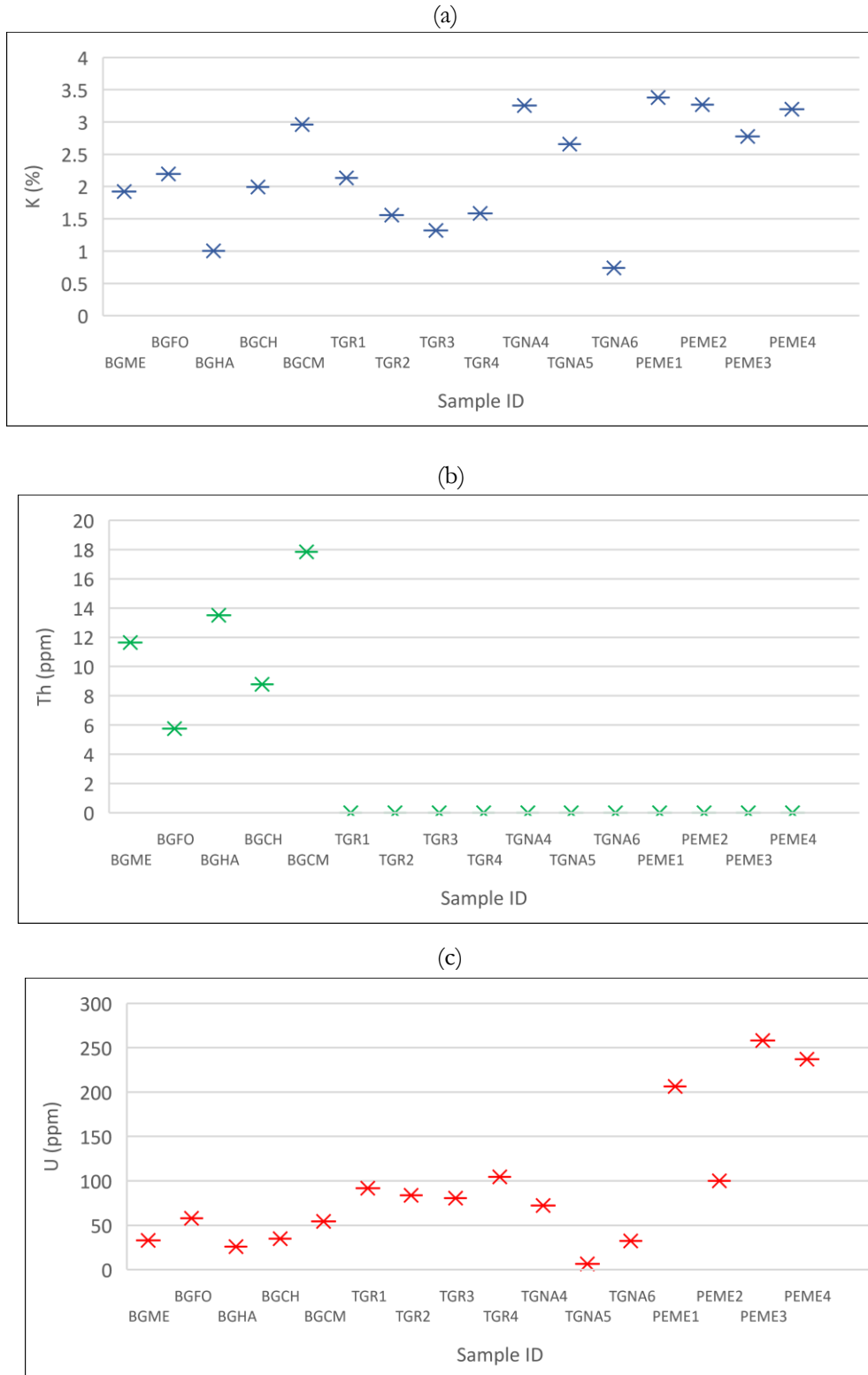
(a)

(b)

(c)

Figure 4.2: Scatterplot of pXRF measured samples against (a) K concentration; (b) Th concentration, and c) U concentration.

4.3. Results of magnetic susceptibility

The relative magnetic susceptibility in the studied samples ranges (from $0.53 * 10^{-3}$ to $1.155 * 10^{-3}$ SI), with a low to moderate magnetic susceptibility value observed in the topaz granite and pegmatite samples (Fig. 4.3) due to the presence of non-magnetic minerals such as topaz, quartz, and feldspars. Similarly, the variation of the values of the magnetic susceptibility is attributed to the presence of ferromagnetic minerals such as biotite. These results can provide a guide for the interpretation of airborne magnetic datasets.
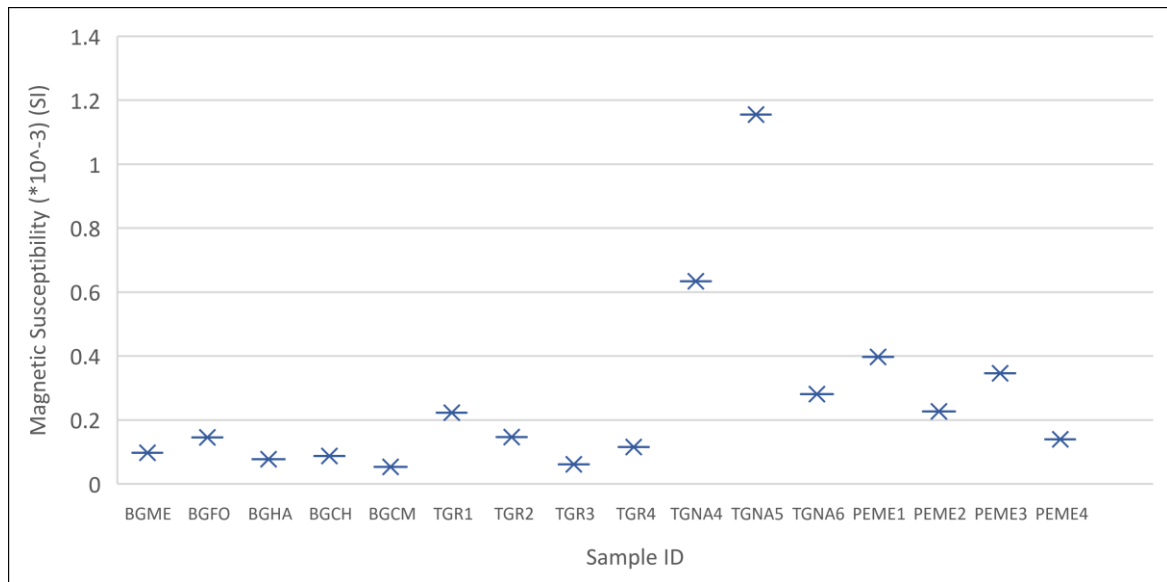

Figure 4.3: Scatter plot of the magnetic susceptibility measurements for batholith granites, topaz granites, and aplite pegmatite samples from Southwestern England. As shown in the plot, batholith granites (BGME, BGFO, BGHA, BGCH, and BGCM) exhibit a very low susceptibility, topaz granite (TGR and TGNA) shows a low to moderate susceptibility, and aplite pegmatite (PEME) exhibits a low susceptibility. These variations show differences in mineral composition.

5.   RESULTS OF AIRBORNE GEOPHYSICAL DATA

This chapter presents the results of airborne geophysical data based on the locations where samples were collected. It is divided into two sections; section 5.1 is the results of the radiometric signatures from the ternary map of SW England. Section 5.2 shows the airborne magnetic signatures of the total magnetic intensity of the region.

5.1.   Results of airborne radiometric data

The airborne radiometric signature from the locations where samples were collected (Fig.5.1) shows whitish for the batholith granite samples (BGFO, BGME, BGHA, BGCH, and BGCM) indicating the presence of the three radioelements potassium, thorium, and uranium. The topaz granite samples (TGNA and TGR) from the Nanpean and Rinsey Cove appear pink showing high values of potassium, and uranium with low thorium concentrations. The aplite pegmatite samples (PEME) appear purple indicating the presence of uranium and potassium with low values of thorium.
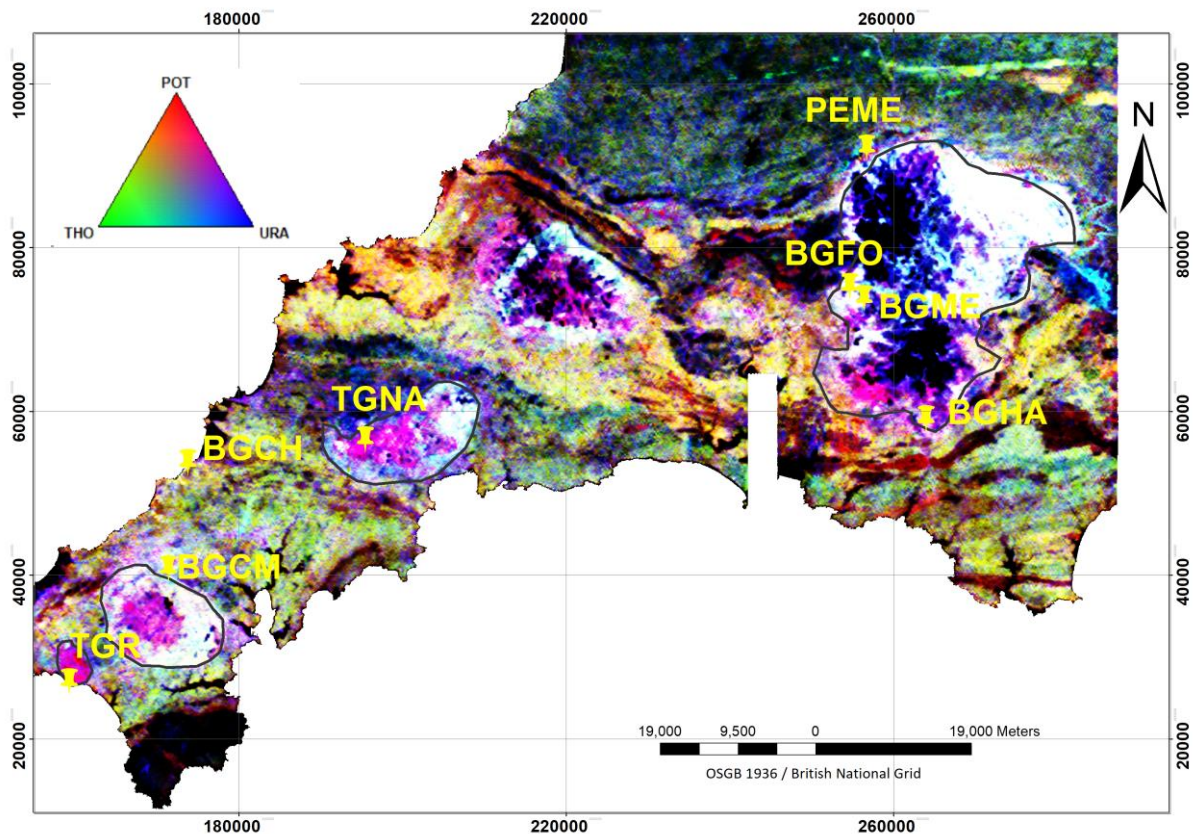

Figure 5.1: Colour-composite 'ternary' image of the airborne radiometric data of Southwestern England from the Tellus SW survey. Sample localities from this study are indicated with yellow markers. The drawn outlines represent the interpretation of the radiometric signature.

Therefore, most of the responses (white color) are found in the outcropping granite zones. In areas where all three radioelement concentrations are low, the ternary image tends to show black; when all three concentrations are high, the ternary image tends to show white. Dartmoor granites have low responses due to significant amounts of peat that form on high ground above them (Beamis, 2014).

5.2. Results of airborne magnetic data

The total magnetic intensity analytical signal (Fig. 5.2) shows batholith granites (BGFO, BGME, BGHA, BGCH, and BGCM) have very weak magnetic anomalies because they contain non-magnetic minerals like biotite, quartz, and feldspar. Due to the large, coherent nature of batholiths, these anomalies are typically broad and continuous. Hence, a weak or moderate magnetic response can indicate the presence of batholith granite. Topaz granites (TGNA and TGR) also show low to moderate magnetic anomalies due to the presence of non-magnetic minerals like topaz, quartz, and feldspar. These anomalies are subtle and could be difficult to differentiate from background noise. Similarly, the aplite pegmatites (PEME) show low to moderate magnetic anomalies which are localized and discontinuous due to the irregular distribution of pegmatite bodies.
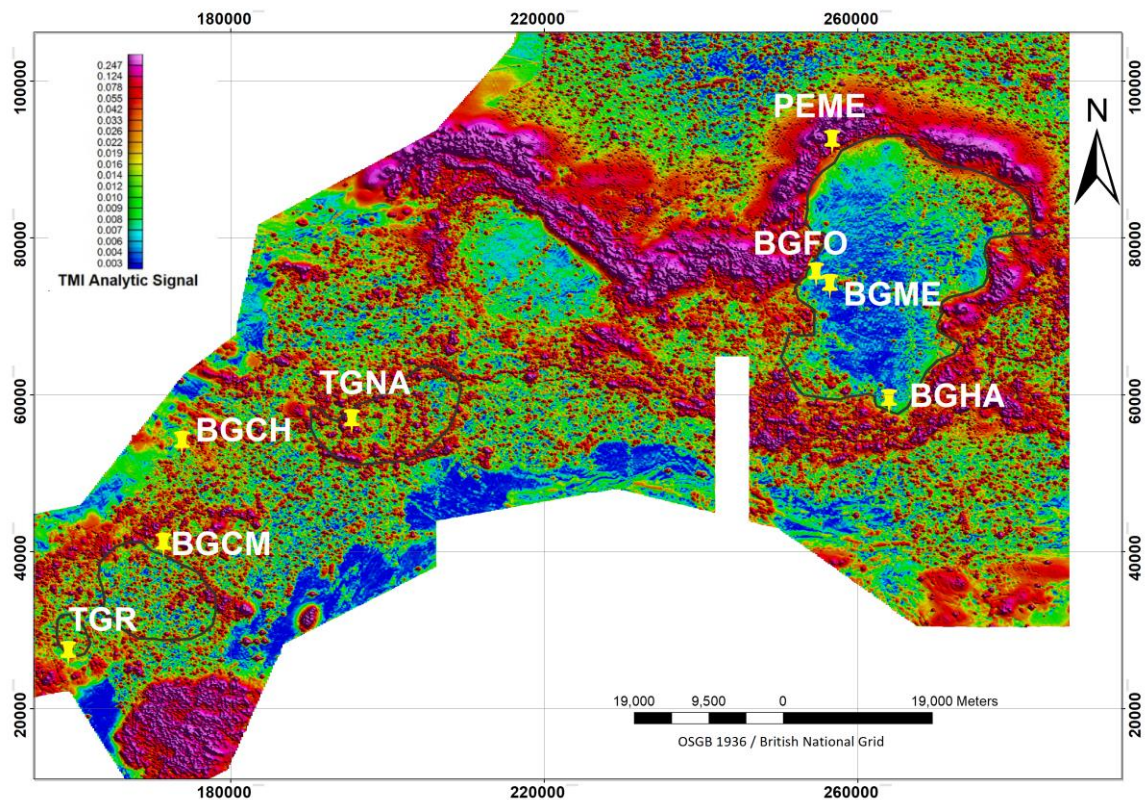

Figure 5.2: Analytical signal image of the airborne magnetic data of Southwestern England from the Tellus SW survey. Sample locations for this study are indicated with yellow markers.

6. INTEGRATION OF RESULTS FROM LABORATORY MEASUREMENTS AND AIRBORNE GEOPHYSICAL DATA

Integrating the results of the laboratory with airborne radiometric and magnetic signatures (Table 6.1) provides a robust approach for the characterization of the geological settings of the lithium-bearing pegmatite system using the spectral characteristics and mineralogy from SWIR imaging spectroscopy, VNIR-SWIR spectroscopy, XRD, XRF, and magnetic susceptibility to identify and describe the small features in the studied samples combined with the airborne radiometric and magnetic datasets.

In the Batholith granite samples, SWIR imaging spectroscopy was used to identify pixels containing tourmaline, illite, and muscovite to differentiate between illite and muscovite across the mineral system. The presence of biotite was observed only in samples BGFO and BGME as found in Appendix VI. The VNIR-SWIR reflectance spectroscopy identified all the minerals present in the samples as muscovite. The XRD analysis was useful for identifying the presence of quartz and feldspars in the studied batholith granite samples, but it was difficult to differentiate the presence of muscovite, illite, biotite, zinnwaldite, and lepidolite. The pXRF results of the batholith granite indicate significant values of the three radioelements potassium, thorium, and uranium (Table 6.1) and correspond with the results from the airborne radiometric signature. The value of magnetic susceptibility is low between 0.061-1.155 and this corresponds with the analytical signal low value of 0.003-0.247 observed from the airborne magnetic signatures. As a result of the magnetization of subsurface materials, the analytical signal detects anomalies in the Earth's magnetic field. The strength of the analytical signal is directly related to the intensity of the magnetic anomalies, so low magnetic susceptibility materials will produce weak magnetic anomalies and weak analytical signals. The

In the topaz granite samples, SWIR imaging spectroscopy identified pixels containing topaz and illite indicating the presence of topaz and illite in the topaz granite samples. The VNIR-SWIR spectroscopy identified the presence of topaz, zinnwaldite, and muscovite in all the topaz granite samples except for sample TGR1 which matches the spectral of an NH4 illite in the USGS spectral library. Similarly, the XRD analysis was useful for identifying the presence of quartz, feldspars, and tourmaline but could not differentiate between the peaks for muscovite/illite/zinnwaldite. The pXRF results show low thorium concentration in all the topaz granite and pegmatite samples which corresponds with the airborne radiometric signature but differs in terms of the high uranium concentration recorded by the pXRF. This could be due to the high concentration of rubidium that affects the x-ray peak by measuring high uranium concentration in the topaz granite and pegmatite samples even when there is no uranium concentration.

The magnetic susceptibility shows low to moderate values (0.634-1.155) in samples TGNA4 and TNGA5 and low in the other topaz granite samples. These correspond with the low magnetic anomalies (0.014-0.0078) values of the analytical signal from airborne magnetic data.

In the pegmatite samples, the SWIR imaging spectroscopy identified pixels containing topaz, illite, muscovite, and tourmaline except for sample PEME4. The VNIR-SWIR spectroscopy identified the presence of topaz, zinnwaldite, and muscovite in all the studied pegmatite samples with the absorption feature of lepidolite in sample PEME3. Furthermore, the XRD analysis could not differentiate between the peaks for muscovite/illite/zinnwaldite but identified the presence of quartz, k-feldspar, tourmaline, and topaz. The airborne radiometric signature shows low thorium concentration with high magnetic susceptibility except for sample PEME4, and this corresponds to the high magnetic signature in the airborne magnetic data.

The pXRF-measured values (0.74-3.38%) of potassium concentration in all the studied samples correspond with (1.13-2.09%) values of the airborne potassium distribution concentration. The pXRF values in the batholith granites were 1-2.96% due to the presence of biotite and the heterogeneity nature of the batholith granite samples, and the more variable potassium concentration (0.74-3.38%) in the topaz granite and pegmatite are due to the presence of topaz and microcline feldspar.

To determine quantitively the values of potassium, thorium, and uranium concentrations the values of the individual channels were extracted from the color legend of the already processed Tellus SW airborne geophysical survey and can be found in Appendix VIII.

Table 6.1: Integration of laboratory and airborne geophysical datasets. **Note** <dl: below detection limit

S/N	Component	Sample ID	Spectral mineralogy SWIR imaging spectroscopy	Bulk mean spectrum (HALO)	XRD (mineralogy)	pXRF			Relative magnetic susceptibility (*10⁻³ SI)	Airborne radiometric signature			Airborne magnetic signature (analytical signal)
						K (%)	Th (ppm)	U (ppm)		K (%)	Th (ppm)	U (ppm)	
1.	batholith granite	BGCH (G2)	tourmaline, illite, muscovite	muscovite	quartz, tourmaline, muscovite/illite/biotite, K-feldspar	1.99	8.8	57.72	0.087	1.13-1.19	2.88-5.11	2.72-3.36	0.014-0.016
		BGCM (G2)	tourmaline, illite, muscovite	muscovite	quartz,tourmaline, muscovite/illite/biotite, K-feldspar	2.96	17.8	54.46	0.053	>2.09	9.59-9.89	>3.36	0.022-0.026
		BGME (G3a)	tourmaline, illite	muscovite	quartz,biotite,tourmaline, muscovite/illite, K-feldspar	1.92	11.7	32.81	0.097	>2.09	10.76-11.64	>3.36	0.055-0.078
		BGFO (G3a)	tourmaline, biotite, illite	muscovite	quartz, tourmaline, muscovite/illite/biotite, K-feldspar	2.19	5.8	26.01	0.145	>2.09	>11.64	>3.36	0.003-0.004
		BGHA (G3b)	tourmaline, illite, biotite	muscovite	quartz, tourmaline, muscovite/illite/biotite, K-feldspar	1.00	13.5	34.78	0.077	>2.09	9.89-10.27	> 3.36	0.007-0.008
2.	topaz granite	TGNA4 (G5a)	topaz, illite, zinnwaldite	topaz, muscovite, zinnwaldite	quartz, muscovite/illite/zinnwaldite, tourmaline, topaz, K-feldspar	3.26	<dl	72.38	0.634	>2.09	2.88-5.11	2.72-3.36	0.055-0.078
		TGNA5 (G5a)	topaz, illite, zinnwaldite	topaz, muscovite, zinnwaldite	quartz, muscovite/illite/zinnwaldite, tourmaline, topaz, K-feldspar	2.66	<dl	6.43	1.155	>2.09	2.88-5.11	2.72-3.36	0.055-0.0078
		TGNA6 (G5a)	topaz, illite, zinnwaldite	topaz, muscovite, zinnwaldite	quartz, muscovite/illite/zinnwaldite, tourmaline, topaz, K-feldspar	0.74	<dl	32.36	0.281	>2.09	2.88-5.11	2.72-3.36	0.055-0.078
		TGR1 (G5a)	topaz, NH4 illite, zinnwaldite	topaz, NH4 illite, zinnwaldite	quartz, muscovite/illite/zinnwaldite, tourmaline, topaz, K-feldspar	2.13	<dl	91.73	0.223	1.19-1.25	2.88-5.11	>3.36	0.014-0.016

		TGR2 (G5a)	topaz, illite, zinnwaldite	topaz, muscovite, zinnwaldite	quartz, muscovite/illite/zinnwaldite, tourmaline, topaz, K-feldspar	1.56	<dl	83.78	0.146	1.19-1.25	2.88-5.11	>3.36	0.014-0.016
		TGR3 (G5a)	topaz, tourmaline, illite, zinnwaldite	topaz, muscovite, zinnwaldite	quartz, muscovite/illite/zinnwaldite, tourmaline, topaz, K-feldspar	1.32	<dl	80.56	0.061	1.19-1.25	2.88-5.11	>3.36	0.014-0.016
		TGR4 (G5a)	topaz , tourmaline, illite, zinnwaldite	topaz, muscovite, zinnwaldite	quartz, muscovite/illite/zinnwaldite, tourmaline, topaz, K-feldspar	1.59	<dl	104.48	0.115	1.19-1.25	2.88-5.11	>3.36	0.014-0.016
3.	aplite pegmatite	PEME1 (G5b)	muscovite, illite, topaz, turmaline, zinnwaldite	topaz, muscovite, zinnwaldite	quartz, muscovite/illite/zinnwaldite, tourmaline, topaz, K-feldspar	3.38	<dl	206.41	0.397	1.69-1.79	>11.64	2.72-3.36	>0.247
		PEME2 (G5b)	muscovite, illite, topaz, turmaline, zinnwaldite	topaz, muscovite, zinnwaldite	quartz, muscovite/illite/zinnwaldite, tourmaline, topaz, K-feldspar	3.27	<dl	100.04	0.227	1.69-1.79	>11.64	2.72-3.36	>0.247
		PEME3 (G5b)	muscovite,illite,topaz,turmaline, zinnwaldite	topaz, muscovite, zinnwaldite and lepidolite	quartz, muscovite/illite/zinnwaldite, tourmaline, topaz, K-feldspar	2.78	<dl	258.10	0.346	1.69-1.79	>11.64	2.72-3.36	>0.247
		PEME4 (G5b)		topaz, muscovite and zinnwaldite	quartz, muscovite/illite/zinnwaldite, tourmaline, topaz, K-feldspar	3.19	<dl	237.04	0.139	1.69-1.79	>11.64	2.72-3.36	>0.247

The descriptive multi-observable model (Fig. 6.1) combines all the diverse datasets to characterize the lithium-bearing pegmatite system to enhance an understanding of the identification and characteristics of the different rock types in the mineral system.
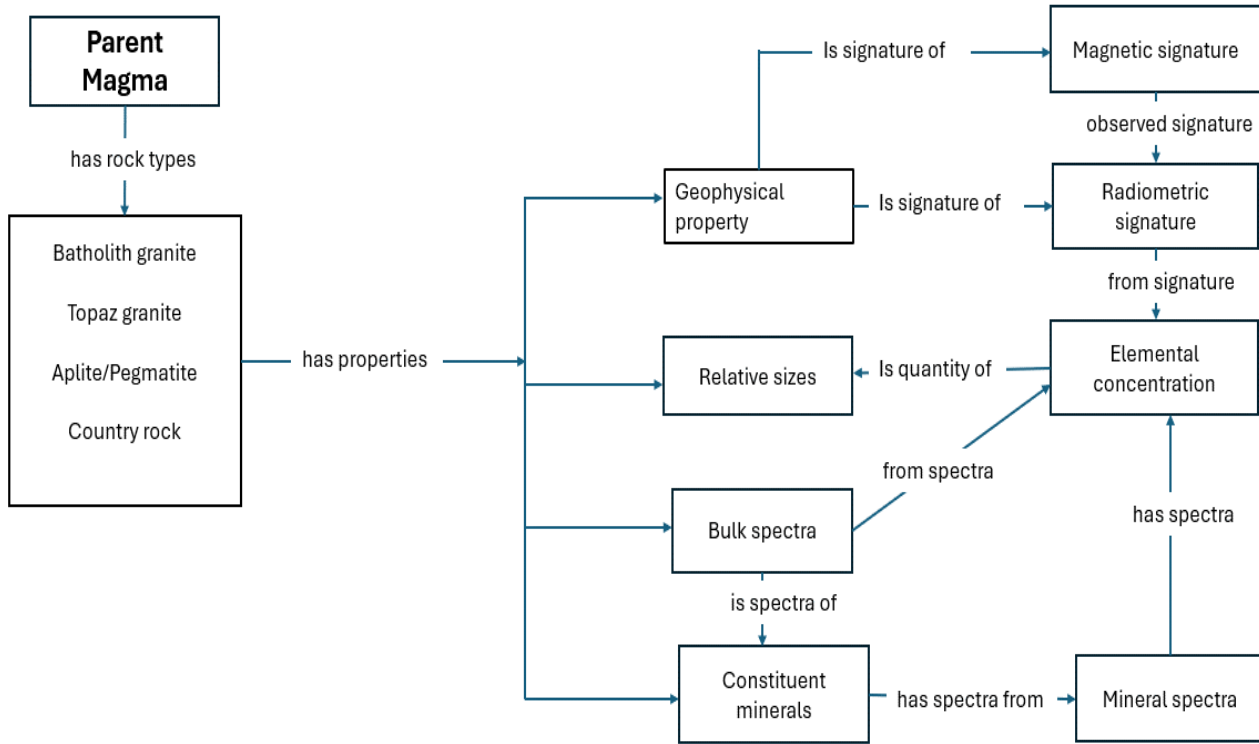

Figure 6.1: Descriptive multi-observable model

7. DISCUSSION, CONCLUSION AND RECOMMENDATIONS

This chapter presents the discussion, conclusions, and recommendations based on the results of these studies. Section 7.1 provides a discussion of the results; Section 7.2 describes the conclusions; and Section 7.3 provides recommendations from the findings for future research.

7.1. Discussion of results

This research used data acquired from laboratory measurements; SWIR imaging spectroscopy and VNIR-SWIR reflectance spectroscopy to analyze the spectral characteristics and XRD, XRF, and magnetic susceptibility which could detect the smaller features in the studied samples to determine the mineralogy with a combination of the airborne radiometric and magnetic data for detecting the larger features in the lithium-bearing pegmatite system. The XRF and magnetic susceptibility were combined for comparison with the airborne magnetic and radiometric signatures.

Batholith granites, topaz granites, and aplite-pegmatites, while distinct in their specific compositions and textures, often form part of a continuum within a single magmatic system, showing changes due to progressive magmatic differentiation. The results of the SWIR imaging spectroscopy of the batholith granites typically show spectral signatures indicative of muscovite, illite, tourmaline, and biotite (Fig. 3.1-3.4), while the topaz granite is characterized by the presence of illite, muscovite, tourmaline, and topaz with a distinct absorption feature at 2079-2086 nm in the wavelength map (Appendix III). Reflectance spectra in VNIR-SWIR ranges highlight the presence of minerals like muscovite in all the studied batholith granite samples due to the presence of Fe absorption features in the VNIR range of the spectrum (Fig.3.13a). In the topaz granite samples, the VNIR-SWIR spectra indicate the presence of topaz at 2083-2086 nm and other lithium-bearing minerals (zinnwaldite) in the VNIR range of the spectrum due to the presence of Fe (Fig.3.15a). A shift in the Al-OH absorption features is noticeable in the 2200 nm range of the spectrum. In all pegmatite samples, zinnwaldite shows a distinct absorption feature at 861-887 nm, except for PEME3 with lepidolite, which shows a distinct absorption feature at 574 nm due to Fe or Mn (Table 3.2).

The XRD patterns show predominant peaks for quartz, feldspars, tourmaline, biotite/muscovite/illite in all the studied batholith granite samples. The XRD results of the topaz granite include peaks due to topaz, with additional peaks for quartz, feldspars, and the presence of zinnwaldite/illite/muscovite in the studied samples. The XRD results of the pegmatite reveal peaks for quartz, feldspars, tourmaline, zinnwaldite/illite/muscovite/lepidolite, and topaz with well-defined crystallinity.

The magnetic susceptibility result indicates very low magnetic susceptibility in batholith granites due to the presence of ferromagnesian minerals like biotite because granites with high concentrations of such

ferromagnesian minerals, high in quartz and feldspars will have lower magnetic susceptibility (Fig.4.3). A low to moderate magnetic susceptibility in topaz granites could be due to the presence of non-magnetic minerals such as topaz, quartz and feldspar and the iron associated with zinnwaldite. The low magnetic susceptibility observed especially in lithium-rich pegmatites is due to the low concentration of ferromagnetic minerals and the high degree of fractionation compared to the less evolved batholith granites.

Similarly, all the studied rock samples from batholith granite, topaz granite, and aplite pegmatite share common primary minerals quartz, feldspar, and tourmaline but differ in accessory minerals, due to varying degrees of fractionation. The batholith granites in terms of texture are typically coarse-grained, transitioning from medium-grained in the topaz granite to fine-grained aplite and very coarse-grained pegmatites. This textural progression is a direct result of the cooling history and volatile content.

The shift of the wavelength of the deepest absorption feature from a shorter wavelength (2190 nm) mostly from the aplite pegmatite, topaz granite, and batholith granite to a longer wavelength (2210 nm) (Fig. 3.10), presence, and abundance of topaz in the topaz granite and aplite pegmatites (Appendix IV), absence of topaz in the batholith granites (Appendix VI) and the presence of biotite in the G3 granites (Appendix VI) reveal the transition among batholith granites, topaz granites, and aplite-pegmatites. These variations reflect the progressive fractionation of the parent magma, with each analytical technique contributing unique insights into the mineralogical, geochemical, and geophysical properties of these rock types.

The G1-G5 classification by Simon et al. (2016; 2017) categorized granite samples based on their geochemical and mineralogical composition. This provides an understanding of the differentiation and evolution processes of the lithium-bearing pegmatite system. Based on the results of this study, the XRD patterns show dominant peaks of quartz, feldspars (k-feldspar and plagioclase), and tourmaline in all the samples. The presence of the at peak at 8-9° 2θ due to biotite/muscovite/illite/muscovite and zinnwaldite (Fig.4.1) made it challenging to distinguish which of these minerals are present and the topaz peak at 24°, 26°, 28° and 31° 2θ indicating the presence of topaz in all the studied samples differs slightly based on the presence of topaz only in the G2, G4 and G5 by Simons et al. (2016; 2017) which could be due to the sensitivity of shifts in the XRD peaks.

The spectral results used distinct absorption features due to Al-OH, Fe-OH, and Mg-OH to identify and distinguish the presence of tourmaline and aluminous-bearing micas; muscovite, and illite in all the studied samples. The presence of diagnostic absorption features in the wavelength map ranging from 2248-2253 nm due to Fe-OH in the G3 (Appendix IV) shows the presence of biotite except in sample BGME (G3a). The presence of the feature at 2083 nm and pixels containing topaz in (Appendix III) shows the presence of topaz only in all the topaz granite and pegmatite samples and these differ from the inclusion of topaz as an accessory mineral in G2 granite classification by Simons et al. (2016). And the G2 and G3 granites show more absorption features attributed due to illite. Illite as a secondary alteration mineral should not be

included as a primary classification of the G1-G5 granite classification but can be analyzed and documented to provide evidence of the level of hydrothermal alteration, weathering processes, and history of the rock types which can provide useful information for geological mapping and mineral exploration.

Based on XRD and spectral results, the G3 granites are highly fractionated and enriched in rare elements, which is consistent with the G3 classification by Simons et al. (2016). The presence of biotite, tourmaline, and the absence of topaz and their distinct spectral features support this classification. Therefore, the classification by Simons et al. (2016) for G3 granites aligns well with the results obtained from XRD and spectral methods.

Spectral methods, particularly VNIR-SWIR reflectance, and imaging spectroscopy, are effective for identifying specific lithium-bearing minerals (zinnwaldite and lepidolite), making them useful for classifying highly fractionated granites (G3, G5). The exploration of highly fractionated granites particularly G3 and G5 is of economic importance due to their enrichment in lithium and other critical rare-earth minerals. These methods provide rapid, non-destructive analysis and can cover large areas, making them suitable for preliminary field assessments and remote sensing applications. There is significant potential to classify granites using remote sensing, especially for identifying and mapping highly fractionated granites with distinct spectral features. Remote sensing techniques can complement ground-based methods by providing a broader geological context and identifying areas of interest for detailed exploration. While spectral methods are powerful for mineral identification and mapping, they might miss subtle geochemical variations that pXRF or detailed geochemical analysis would reveal. However, Fig. 7.1 illustrates a good example of a topaz granite sample (TGR2) showing the presence of zinnwaldite with distinctive absorption features at 2210 and 2247 nm. To qualitatively determine the mineral composition of each rock sample, the decision tree classification in Appendix VII was useful in providing information on the mineralogy of each rock sample and shows pixels containing aluminous micas and zinnwaldite. However, the classification does not account for mineral mixtures, and this could result in missing end members.

On the other hand, XRD provides mineralogical composition, but it is limited to sample analysis and is not suitable for large-scale mapping. Spectral methods reveal surface mineralogy and can indicate alteration zones and mineral distributions. pXRF and XRD provide geochemical and mineralogical data, crucial for understanding the complete geological history and classification.
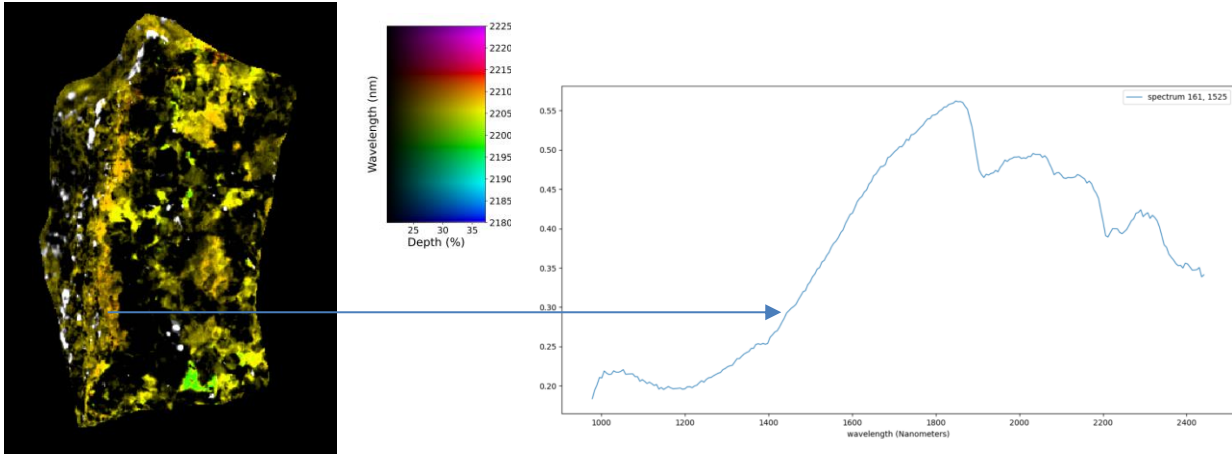
Figure 7.1: Example of a sample indicating the presence of lithium-bearing mica (zinnwaldite)

The G1-G5 classification by Simons et al. (2016) works well with XRD and spectral results, particularly for highly fractionated granites like G3 granites. Spectral methods are useful for classifying granites, especially when combined with XRD and XRF data, providing a comprehensive understanding of granite systems. Remote sensing has strong potential for classifying and mapping granites, complementing traditional geological methods, and enhancing exploration efficiency.

For the evaluation of the results of these studies, chemical data from Simons et al. (2016, 2017) was compared with the results of the portable XRF to provide a baseline on the K, U, and Th concentrations of the studied samples and show the level of accuracy using the pXRF. These elements are critical for the analysis of radiometric signatures and play a significant role in the geochemical characterization of different rock types.

In fig. 7.2, the scatterplot of uranium against potassium shows a high uranium value from the pXRF data from this study when compared with the uranium concentration from Simons et al. (2017), which is due to the high concentration of pegmatites with rubidium that interferes with the characteristics x-ray peak of uranium. However, there are no noticeable trends observed in the different rock types.

Similarly, the scatterplot of thorium against potassium (Fig. 7.3) shows a positive correlation from the results of pXRF and suggests that the thorium concentration is low in the topaz granite and pegmatite which is consistent with previous studies by Simons et al. (2016, 2017) which could suggest the presence of more feldspars in G3 and G5 due to high magmatic fractionation.
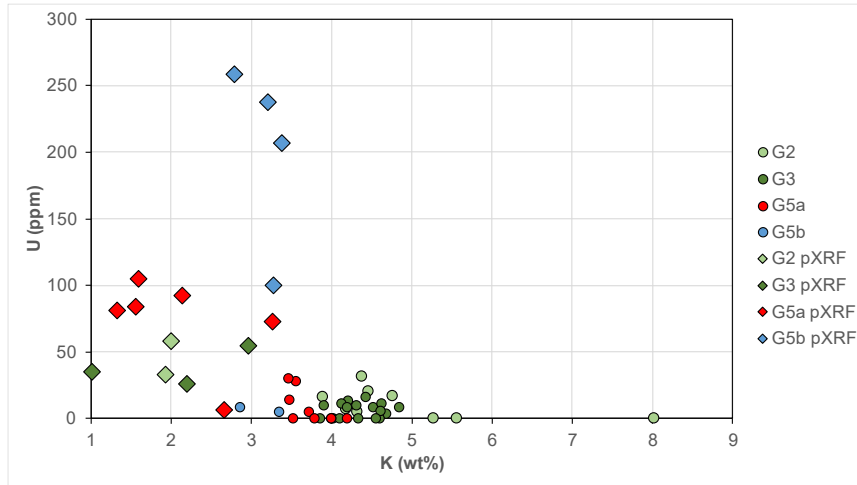
Figure 7.2: Scatterplot of uranium against potassium concentration. Circles represent data from Simons et al. (2016, 2017). Diamonds represent portable XRF measurements from this study. G2 and G3 granites are batholith granites; G5a are topaz granites; G5b are aplite-pegmatites.
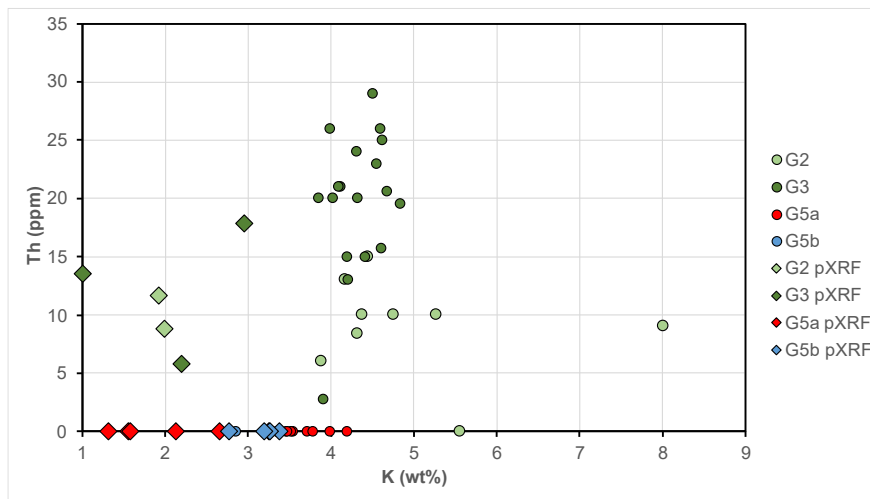
Figure 7.3: Scatterplot of thorium against potassium. Circles represent data from Simons et al. (2016, 2017). Diamonds represent portable XRF measurements from this study. G2 and G3 granites are batholith granites; G5a are topaz granites; G5b are aplite-pegmatites.

These trends underscore the genetic relationship among these rock types and enhance the understanding of the evolution of the magmatic system, aiding in targeted exploration and characterization of lithium-bearing pegmatite systems. Based on the analysis of the results from this study, the batholith granites show the absence of lithium-bearing minerals, with the topaz granite containing increased lithium-bearing minerals like zinnwaldite although still relatively in low quantities (Appendix VII). The highly fractionated aplite-pegmatite shows a high lithium concentration enriched with zinnwaldite and lepidolite. This increase or absence in lithium concentration from batholith granite to topaz granite to aplite pegmatite reflects the trend in magmatic fractionation in which lithium becomes increasingly concentrated in the residual melts.

7.2.   Conclusion

This research combined the analysis of spectral characteristics and airborne geophysical signatures to develop a descriptive multi-observable model for identifying and describing a lithium-bearing pegmatite system. In these studies, the leucogranite component of the lithium-bearing pegmatite system was not considered. The study employed an integration approach using SWIR imaging spectroscopy, VNIR-SWIR reflectance spectroscopy, XRD, and XRF with airborne radiometric and magnetic signatures. Based on the results and discussions above, the SPECIM imaging spectroscopy in the SWIR range was found to be effective in identifying the different aluminous micas, tourmaline, topaz, and biotite but could not map or identify non-active SWIR minerals such as quartz and feldspars. The VNIR-SWIR reflectance spectroscopy on the other hand was successful in identifying minerals like Li-bearing micas lepidolite and zinnwaldite due to the distinct absorption features of Fe or Mn in the VNIR range of the spectrum, although it is a point measurement and does not account for the entire surface area of the studied samples.

The XRD method was effective in identifying the presence of quartz and alkaline feldspar-like albite which could prove difficult to identify using SPECIM imaging spectroscopy. The results from the portable XRF could not identify lithium concentration and the high uranium concentration recorded by the instrument due to rubidium showed the limitations of using pXRF.

The airborne magnetic and radiometric signatures were effective for identifying the larger features in the different components of the system and provided insight into the mineralogy and magnetic relief of the rock samples. This research identifies the discrepancies in using the various methods for the identification and description of the lithium-bearing pegmatite system.

Based on this study, recognizing a lithium pegmatite system using spectral, magnetic, and radiometric data can be approached through both remote sensing and proximal sensing techniques. Remote sensing using airborne magnetic and radiometric data can cover larger areas, identifying lithium-bearing pegmatite systems based on their magnetic and radiometric signatures. However, the resolution of the remote sensing data can limit the smaller features or deeply buried pegmatite bodies. On the other hand, proximal sensing using laboratory-based hyperspectral imaging and reflectance spectroscopy can provide detailed and higher resolution essential for the early exploration of lithium pegmatite systems especially in areas where remote sensing data is insufficient. The integration of these methods can provide a comprehensive framework for identifying and characterizing lithium-bearing pegmatite systems with a particular focus on identifying topaz granites, which are significant indicators due to their size and distinct absorption features at 2083 nm and notable absorption features around 2200 nm due to the Al-OH bonds.

Therefore, to effectively recognize lithium-bearing pegmatite systems, the key component of the system to focus on is the topaz granites because they are large enough to be detected and are identified by the presence of topaz. The presence of topaz in the topaz granites can be characterized using remote sensing radiometric

signature to show the regional overview, SWIR imaging spectroscopy to show the surface mineralogy, and the VNIR-SWIR reflectance spectroscopy can identify the lithium-bearing minerals in the topaz granite. Topaz granites typically exhibit low magnetic susceptibility which can be distinguished from the surrounding rocks. The low thorium concentration from the radiometric data is indicative of the presence of topaz granites and associated aplite pegmatites.

7.3. Recommendations

Based on the results of this study, the author suggests the following recommendations:

- For improved analysis of the spectral characterization and mineralogy, a full spectrum covering the VNIR to the LWIR with a hyperspectral sensor of high spectral resolution should be considered to improve the detection and discrimination of lithium-bearing minerals.

- A need for more samples to be collected since these studies were based only on the few samples collected in the ITC laboratory.

- The information from the multi-observable model in this study can be tested in other regions within Europe with the same trend and style of mineralization.

LIST OF REFERENCES

Beamish, D. (2014). Environmental radioactivity in the UK: the airborne geophysical view of dose rate estimates. *Journal of Environmental Radioactivity*, 138, 249-263. https://doi.org/10.1016/j.jenvrad.2014.08.025

Beamish, D, Howard, A S, Ward, E K, White, J, & Young, M E. (2014). Tellus Southwest airborne geophysical data. Natural Environment Research Council, British Geological Survey. Retrieved on 11 January 2023 from https://www.tellusgb.ac.uk/data/airborneGeophysicalSurvey.html.

Breiter, K., Ďurišová, J., Hrstka, T., Korbelová, Z., Galiová, M. V., Müller, A., & Davies, J. A. (2018). The transition from granite to banded aplite-pegmatite sheet complexes: An example from Megiliggar Rocks, Tregonning topaz granite, Cornwall. *Lithos*, 302, 370-388. https://doi.org/10.1016/j.lithos.2018.01.010Get rights and content

British Lithium (n.d). Mineral resource estimate. Retrieved June 27, 2024, from https://imerysbritishlithium.com/lithium-exploration/mineral-resource-estimate/

Cardoso-Fernandes, J., Silva, J., Perrotta, M. M., Lima, A., Teodoro, A. C., Ribeiro, M. A., & Roda-Robles, E. (2021). Interpretation of the reflectance spectra of lithium (Li) minerals and pegmatites: A case study for mineralogical and lithological identification in the Fregeneda-Almendra Area. *Remote Sensing*, 13(18), 3688. https://doi.org/10.3390/rs13183688

Cardoso-Fernandes, J., Santos, D., Rodrigues de Almeida, C., Lima, A., Teodoro, A. C., & GREENPEG Project Team. (2023). Spectral Library of European Pegmatites, Pegmatite Minerals and Pegmatite Host-Rocks–the GREENPEG project database. *Earth System Science Data*, 15(7), 3111-3129. https://doi.org/10.5194/essd-15-3111-2023

Chen, L., Zhang, N., Zhao, T., Zhang, H., Chang, J., Tao, J., & Chi, Y. (2023). Lithium-Bearing Pegmatite Identification, Based on Spectral Analysis and Machine Learning: A Case Study of the Dahongliutan Area, NW China. *Remote Sensing*, 15(2), 493. https://doi.org/10.3390/rs15020493

Clark, R. N., King, T. V., Klejwa, M., Swayze, G. A., & Vergo, N. (1990). High spectral resolution reflectance spectroscopy of minerals. *Journal of Geophysical Research: Solid Earth*, 95(B8), 12653-12680. https://doi.org/10.1029/JB095iB08p12653

Cornish Lithium (n.d). Opportunities for responsible extraction in the UK. Retrieved June 27, 2024, from https://cornishlithium.com/about/why-cornwall/

Dijkstra, A. H., & Hatch, C. (2018). Mapping a hidden terrane boundary in the mantle lithosphere with lamprophyres. *Nature communications*, 9(1), 3770 https://doi.org/10.1038/s41467-018-06253-7

European Union (2020). Study on the EU's list of critical raw materials – Critical raw materials factsheets, Publications Office. https://data.europa.eu/doi/10.2873/92480

Gourcerol, B., Gloaguen, E., Melleton, J., Tuduri, J., & Galiegue, X. (2019). Re-assessing the European lithium resource potential–A review of hard-rock resources and metallogeny. *Ore Geology Reviews*, *109*, 494-519. https://doi.org/10.1016/j.oregeorev.2019.04.015

Hecker, C., van Ruitenbeek, F. J. A., van der Werff, H. M. A., Bakker, W. H., Hewson, R. D., & Van Der Meer, F. D. (2019c). Spectral absorption feature analysis for finding ore: A tutorial on using the

method in geological remote sensing. *IEEE Geoscience and Remote Sensing Magazine,* 7(2), 51–71. https://doi.org/10.1109/MGRS.2019.2899193

Jacob, J. B., Moyen, J. F., Fiannacca, P., Laurent, O., Bachmann, O., Janoušek, V., & Villaros, A. (2021). Crustal melting vs. fractionation of basaltic magmas: Part 2, Attempting to quantify mantle and crustal contributions in granitoids. *Lithos*, 402, 106292. https://doi.org/10.1016/j.lithos.2021.106292

Keyser, W., Müller, A., Knoll, T., Menuge, J. F., Steiner, R., Berndt, J., & Harrop, J. (2023). Quartz chemistry of lithium pegmatites and its petrogenetic and economic implications: Examples from Wolfsberg (Austria) and Moylisha (Ireland). *Chemical Geology*, 630, 121507. https://doi.org/10.1016/j.chemgeo.2023.121507

Kokaly, R. F., Clark, R. N., Swayze, G. A., Livo, K. E., Hoefen, T. M., Pearson, N. C., & Klein, A. J. (2017). *USGS Spectral Library Version 7* data: US geological survey data release. *United States Geological Survey (USGS): Reston, VA, USA, 61*. https://doi.org/10.3133/ds1035

Maghsoudi Moud, F., Deon, F., van der Meijde, M., van Ruitenbeek, F., & Hewson, R. (2021). Mineral interpretation discrepancies identified between infrared reflectance spectra and X-ray diffractograms. *Sensors*, 21(20), 6924. https://doi.org/10.3390/s21206924

Mekonnen S.A (2023). Spectral analysis of lithium-bearing micas with shortwave and longwave infrared spectroscopy [Master's thesis, University of Twente]. Enschede. https://essay.utwente.nl/97094/1/Mekonenn_MGEO_ITC.pdf

Müller, A., Seltmann, R., Halls, C., Siebel, W., Dulski, P., Jeffries, T., & Kronz, A. (2006). The magmatic evolution of the Land's End pluton, Cornwall, and associated pre-enrichment of metals. *Ore Geology Reviews*, 28(3), 329-367. https://doi.org/10.1016/j.oregeorev.2005.05.002

Müller, A., Reimer, W., Wall, F., Williamson, B., Menuge, J., Brönner, M., & Rausa, A. (2023). GREENPEG–exploration for pegmatite minerals to feed the energy transition: first steps towards the Green Stone Age. https://doi.org/10.1144/SP526-2021-189

Price, G. D., Winkle, K., & Gehrels, W. R. (2005). A geochemical record of the mining history of the Erme Estuary, south Devon, UK. Marine pollution bulletin, 50(12), 1706-1712. https://doi.org/10.1016/j.marpolbul.2005.07.016

Rajesh, H. M. (2004). Application of remote sensing and GIS in mineral resource mapping-An overview. *Journal of mineralogical and Petrological Sciences*, 99(3), 83-103. https://doi.org/10.2465/jmps.99.83

Searle, M. P., Shail, R. K., Pownall, J. M., Jurkowski, C., Watts, A. B., & Robb, L. J. (2024). The Permian Cornubian granite batholith, SW England; Part 1: Field, structural, and petrological constraints. Geological Society of America Bulletin. https://doi.org/10.1130/B37457.1

Shail, R. K., Stuart, F. M., Wilkinson, J. J., & Boyce, A. J. (2003). The role of post-Variscan extensional tectonics and mantle melting in the generation of the Lower Permian granites and the giant W-As-Sn-Cu-Zn-Pb ore field of SW England. http://hdl.handle.net/10036/3644

Simons, B., Shail, R. K., & Andersen, J. C. (2016). The petrogenesis of the Early Permian Variscan granites of the Cornubian Batholith: Lower plate post-collisional peraluminous magmatism in the Rhenohercynian Zone of SW England. *Lithos*, 260, 76-94. https://doi.org/10.1016/j.lithos.2016.05.010

Simons, B., Andersen, J. C., Shail, R. K., & Jenner, F. E. (2017). Fractionation of Li, Be, Ga, Nb, Ta, In, Sn, Sb, W and Bi in the peraluminous early permian Variscan granites of the Cornubian Batholith: Precursor processes to magmatic-hydrothermal mineralisation. *Lithos*, 278, 491-512. https://doi.org/10.1016/j.lithos.2017.02.007

Smith, W. D., Darling, J. R., Bullen, D. S., Lasalle, S., Pereira, I. F. G. M., Moreira, H., & Tapster, S. (2019). Zircon perspectives on the age and origin of evolved S-type granites from the Cornubian Batholith, Southwest England. *Lithos*, 336, 14-26. https://doi.org/10.1016/j.lithos.2019.03.025

Sweetapple, M. T. (2017). Granitic pegmatites as mineral systems: Examples from the Archaean. NGF Abstr. Proc, 2, 139-142. Retrieved October 30, 2023 from https://www.researchgate.net/profile/Marcus Sweetapple/publication/319275486_Granitic_pegmatites_as_mineral_systems_examples_from_t he_Archaean/links/599ffaa44585151e3c73d9eb/Granitic-pegmatites-as-mineral-systems-examples-from-the-Archaean.pdf

van Ruitenbeek, F. J. A., Bakker, W. H., van Der Werff, H. M. A., Zegers, T. E., Oosthoek, J. H. P., Omer, Z. A., & van Der Meer, F. D. (2014). Mapping the wavelength position of deepest absorption features to explore mineral diversity in hyperspectral images. Planetary and Space Science, 101, 108–117. https://doi.org/10.1016/j.pss.2014.06.009

van Ruitenbeek, F. J. A., van der Werff, H. M. A., Bakker, W. H., van der Meer, F. D., & Hein, K. A. A. (2019). Measuring rock microstructure in hyperspectral mineral maps. *Remote sensing of environment*, 220, 94-109. https://doi.org/10.1016/j.rse.2018.10.030

Williamson, B. J., Spratt, J., Adams, J. T., Tindle, A. G., & Stanley, C. J. (2000). Geochemical constraints from zoned hydrothermal tourmalines on fluid evolution and Sn mineralization: an example from fault breccias at Roche, SW England. *Journal of Petrology*, 41(9), 1439-1453. https://doi.org/10.1093/petrology/41.9.1439

World Bank (2020). Mineral Production to Soar as Demand for Clean Energy Increases Retrieved June 26, 2023 from https://www.worldbank.org/en/news/press-release/2020/05/11/mineral-production-to-soar-as-demand-for-clean-energy-increases

Zimanovskaya, N. A., Oitseva, T. A., Khromykh, S. V., Travin, A. V., Bissatova, A. Y., Annikova, I. Y., & Aitbayeva, S. S. (2022). Geology, Mineralogy, and Age of Li-Bearing Pegmatites: Case Study of Tochka Deposit (East Kazakhstan). *Minerals*, 12(12), 1478. https://doi.org/10.3390/min12121478

APPENDICES

APPENDIX I: List of samples collected from the various locations in the Southwestern England

S/N	Sample ID	Component	Locality
1.	BGCM	Batholith granite	Carn Marth
2.	BGCH	Batholith granite	Cligga Head
3.	BGME	Batholith granite	Dartmoor- Merrivale and
4.	BGFO	Batholith granite	Dartmoor-Foggintor quarry
5.	BGHA	Batholith granite	Dartmoor- Harford
6.	TGNA4	Topaz granite	Nanpean
7.	TGNA5	Topaz granite	Nanpean
8.	TGNA6	Topaz granite	Nanpean
9.	TGR1	Topaz granite	Rinsey Cove
10.	TGR2	Topaz granite	Rinsey Cove
11.	TGR3	Topaz granite	Rinsey Cove
12.	TGR4	Topaz granite	Rinsey Cove
13.	PEME1	Pegmatite	Meldon
14.	PEME2	Pegmatite	Meldon
15.	PEME3	Pegmatite	Meldon
16.	PEME4	Pegmatite	Meldon

APPENDIX II: Pictures of samples

BGFO
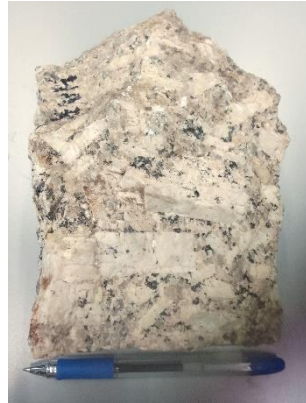
BGHA

BGME

BGCM

BGCH
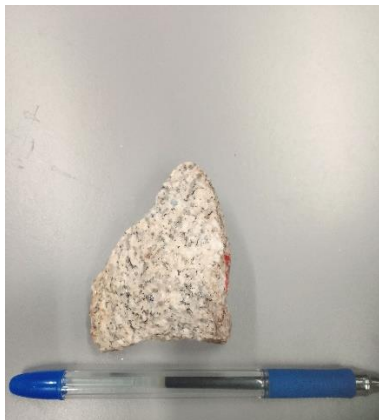
TGR1

TGR2

TGR3

TGR4

TGNA4

TGNA5

TGNA6

PEME1

PEME2

PEME3
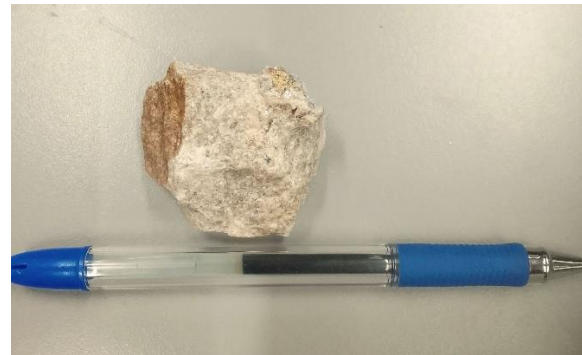
PEME4

APPENDIX III: Samples with the occurrence of muscovite and/or illite (2180 – 2225nm)
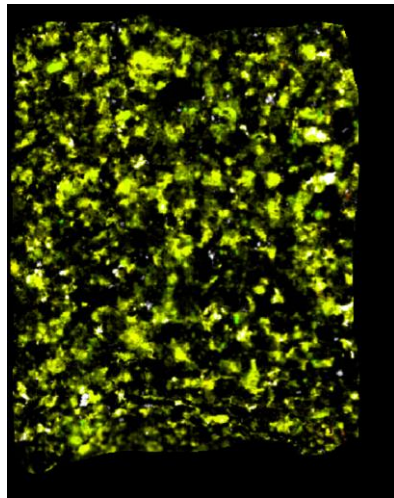
BGFO
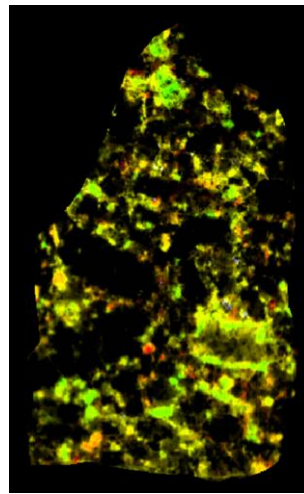
BGHA
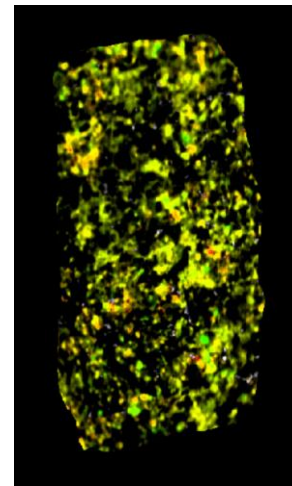
BGME
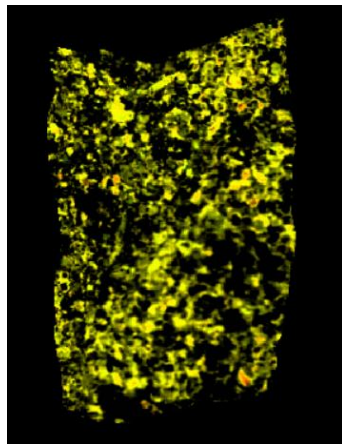
BGCH
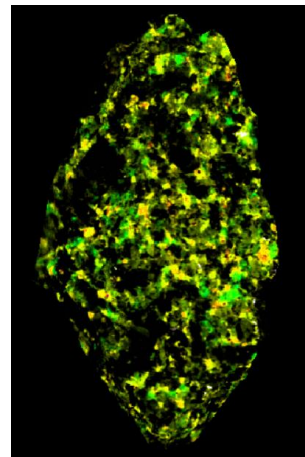
BGCM
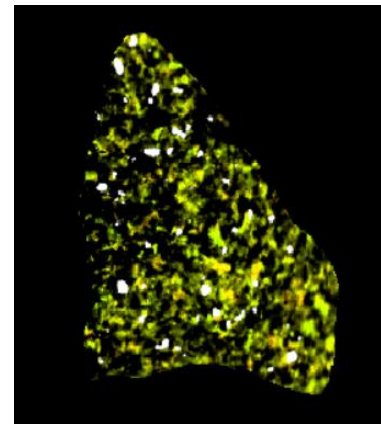
TGR1
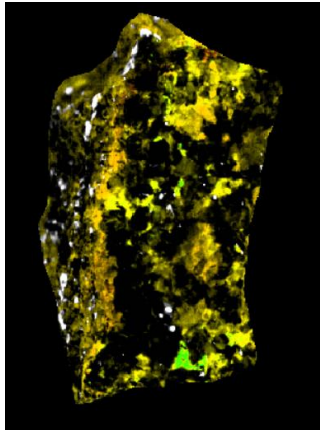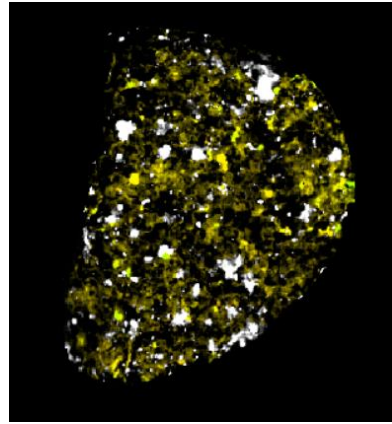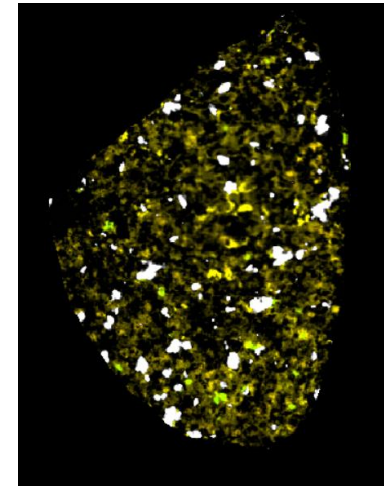
TGR2   TGR3   TGR4
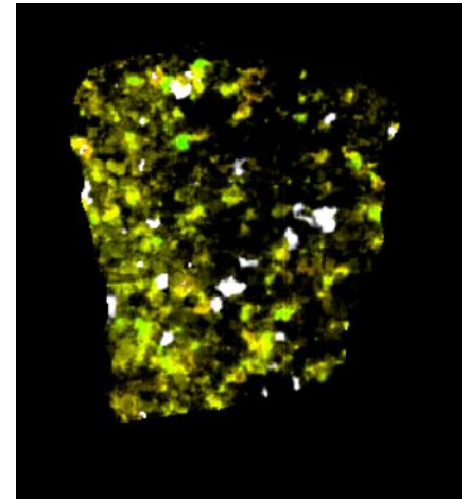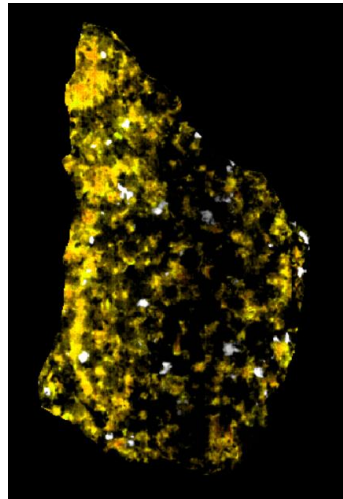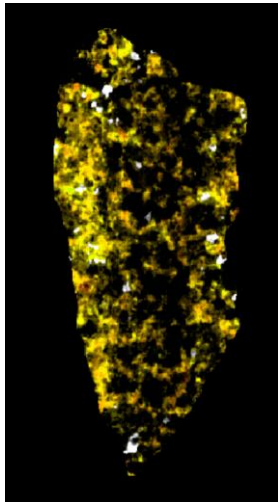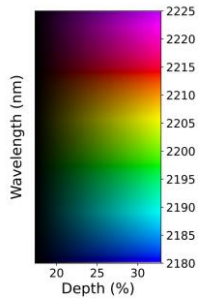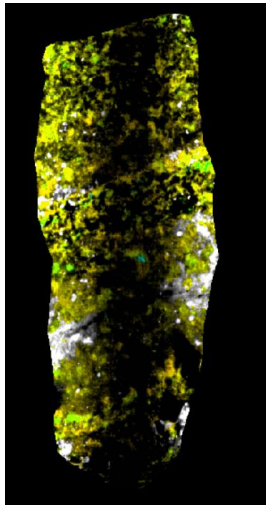
PEME1
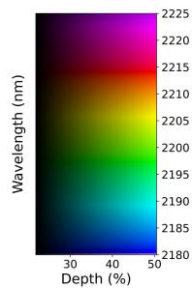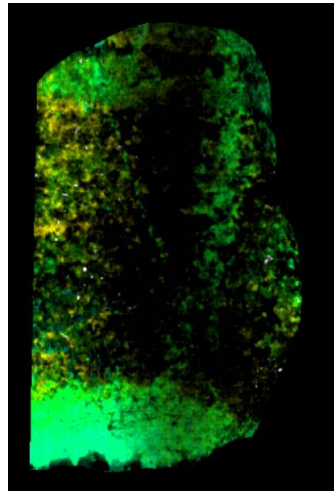
PEME2
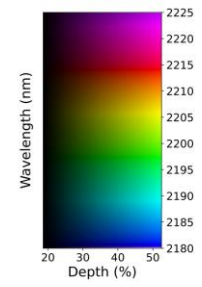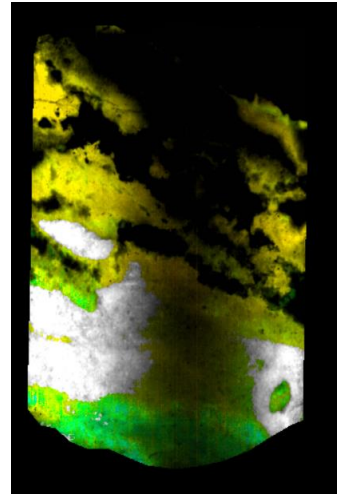
PEME3

APPENDIX IV: Samples with the occurrence of topaz (2079 – 2086nm)
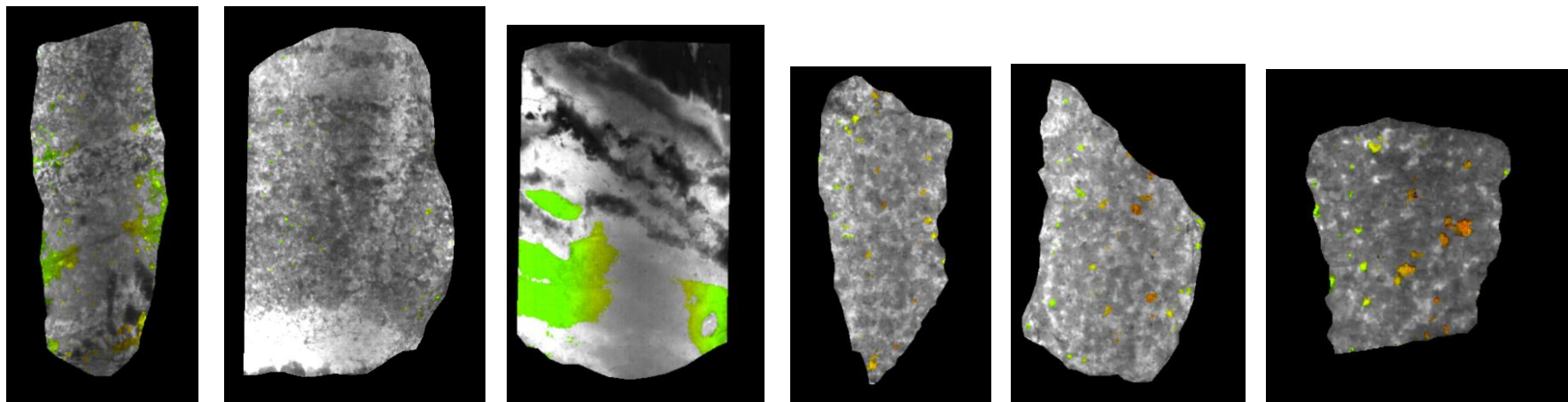
PEME1   PEME2   PEME3   TGNA4   TGNA5   TGNA6
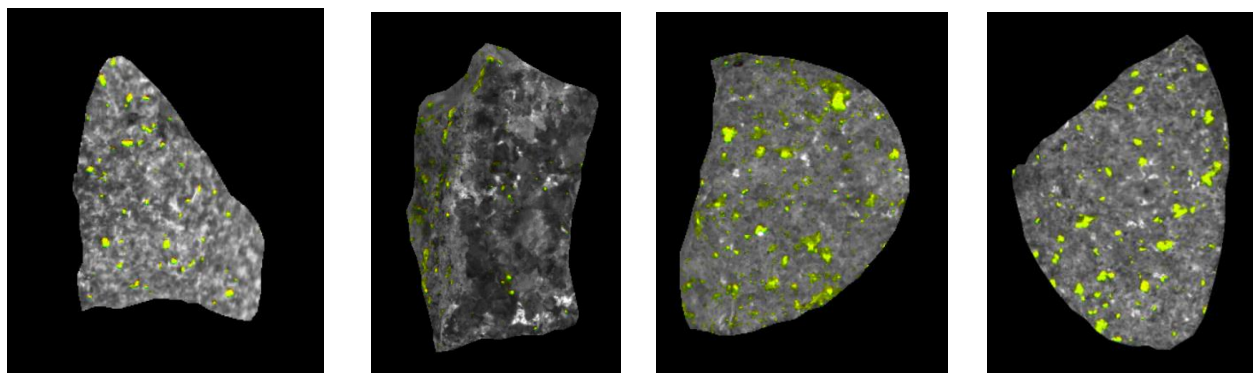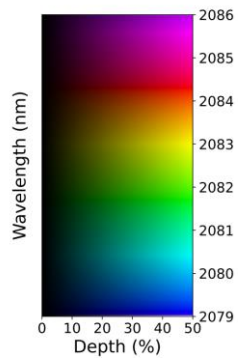
TGR1   TGR2   TGR3   TGR4
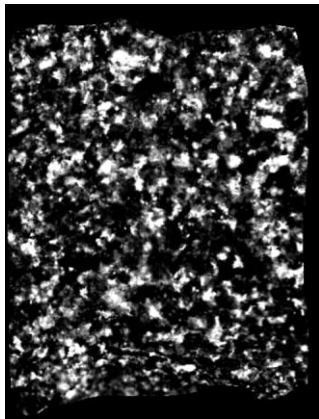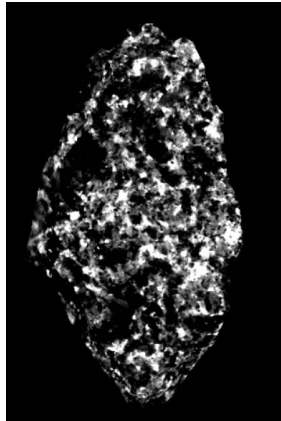
BGFO

BGCH
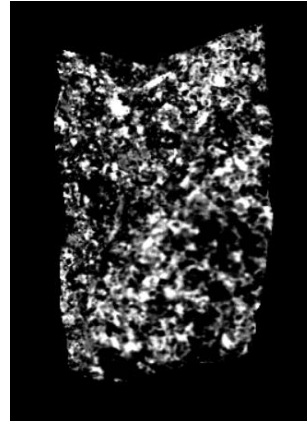
BGCM
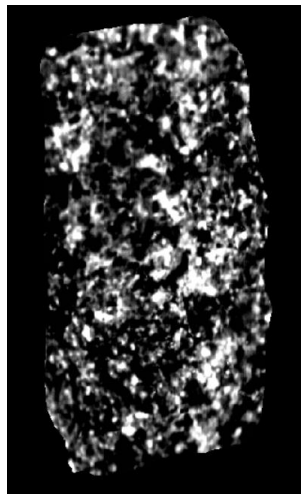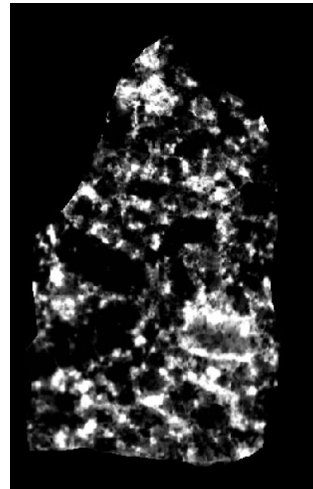
BGHA

BGME

Appendix VI: Samples with the occurrence of biotite (2250 – 2260nm)
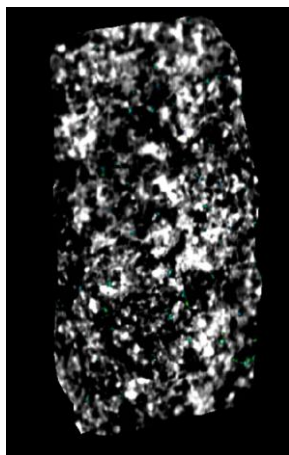
BGHA
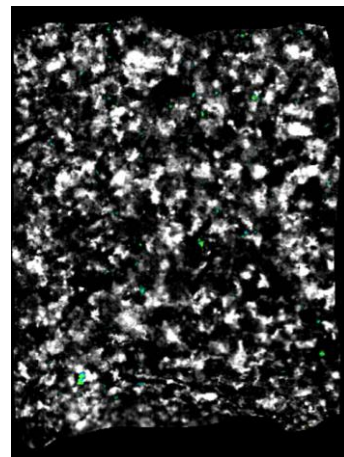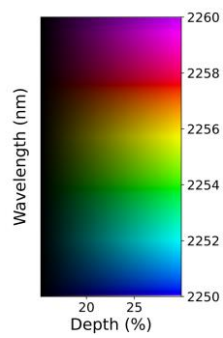
BGFO
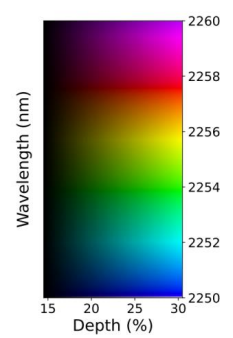
APPENDIX VII: Decision tree classifications for the aluminous micas and zinnwaldite
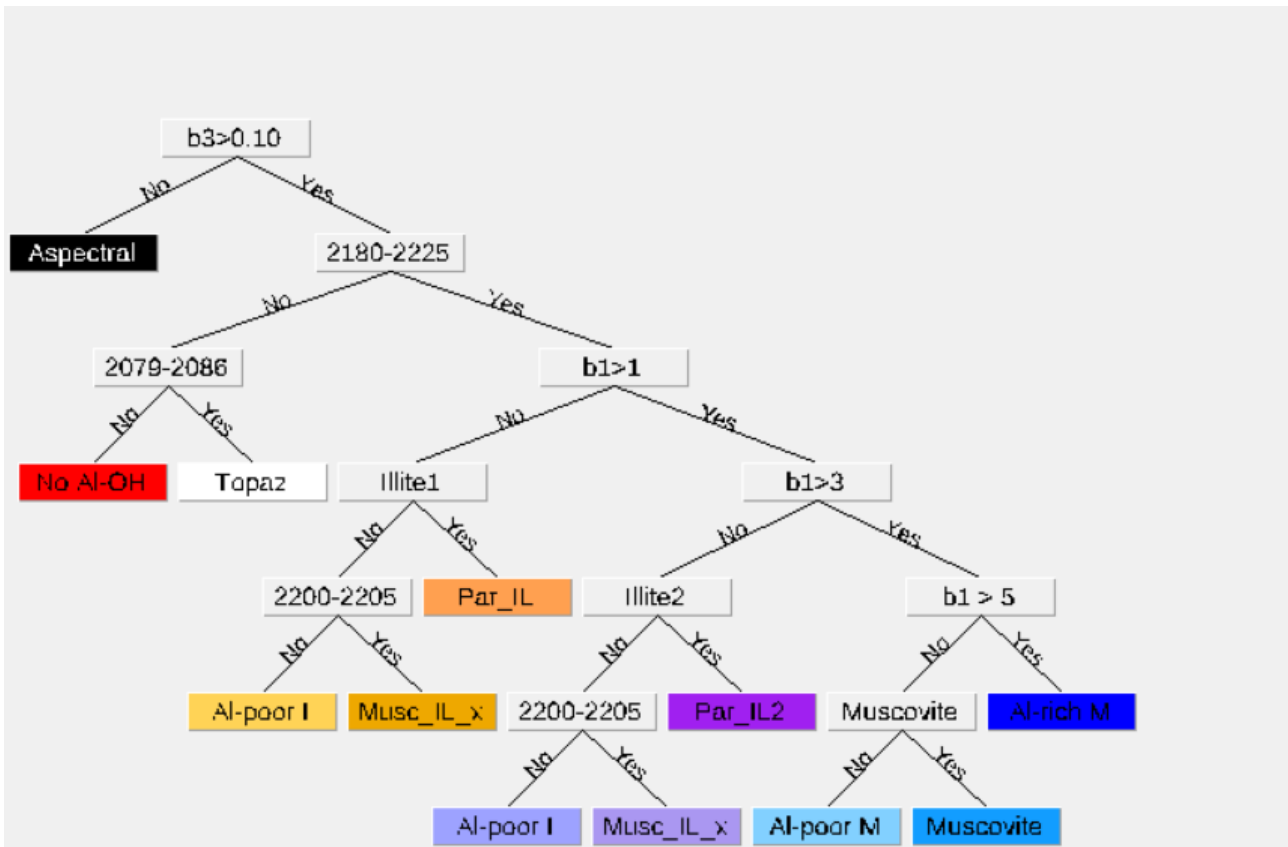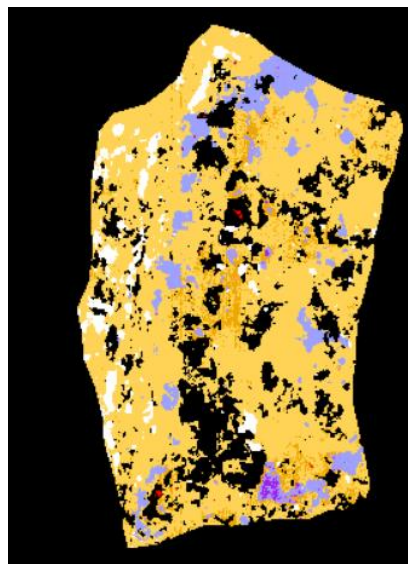

Input parameters:

b1: Illite-muscovite crystallinity

b2: Wavelength of the deepest absorption feature (Al-OH) in the 2100-2400 nm
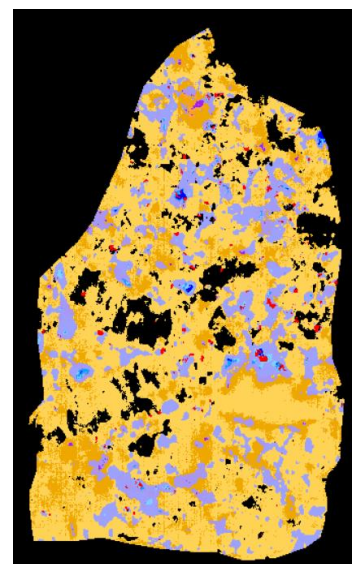
b3: Depth of the deepest absorption feature in the 2100-2400 nm
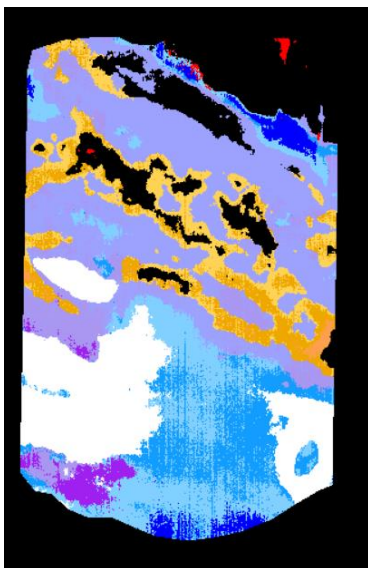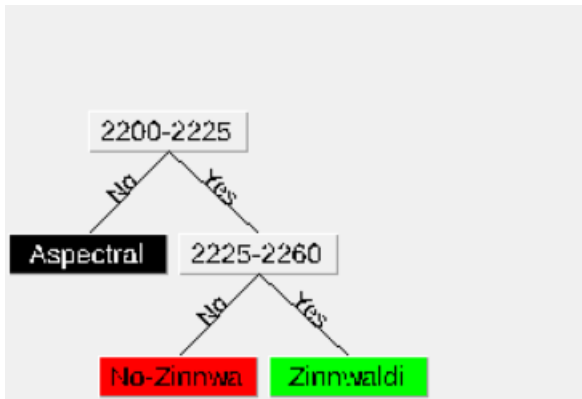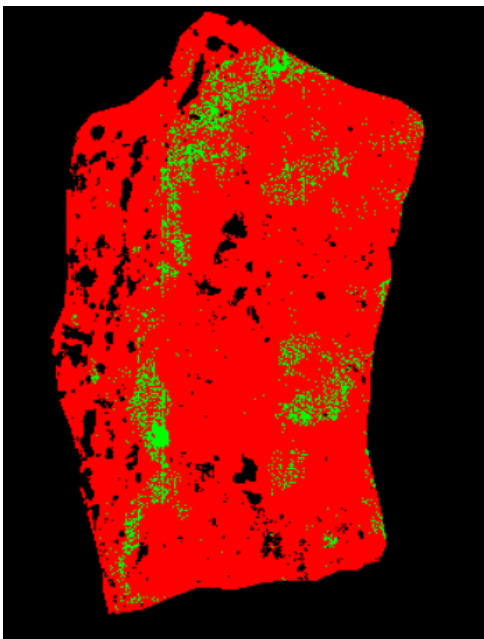

PEME3   TGR2   BGHA
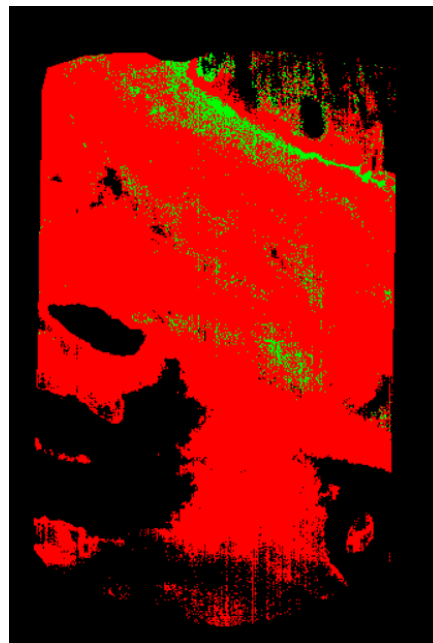
Input Parameters:

b1: Wavelength of the deepest absorption feature (Al-OH) in the 2100-2400 nm

b2: Wavelength of the second deepest absorption feature in the 2100-2400 nm

TGR2

PEME3

Sample ID	Muscovite (%) 2200-2205	Al-poor muscovite (%) 2205-2210 b1>5	Al-poor illite (%) b1>1	Al-poor illite (%) b1>3	Topaz (%)	Zinnwaldite (%)
PEME3	1.07	1.67	0.93	3.02	1.96	0.55
TGR2	-	-	3.66	0.36	0.29	0.41
BGHA	0.03	0.02	1.87	2.76	-	-

Appendix VIII: Concentrations of K, Th, and U from the already processed airborne geophysical data